

Galaxy clusters in the VIDEO fields: detection and characterisation in the context of MOONRISE

P. Galois^{1,*}, C. Benoist¹, G. Castignani², M. Maturi^{3,4}, S. Maurogordato¹, P. Jablonka^{5,6}, Y. M. Bahé^{5,7}, D. J. McLeod⁸, R. A. A. Bowler⁹, O. Cucciati², L. Moscardini^{10,2,11}, M. Magliocchetti¹², M. Radovich⁷, M. Cirasuolo¹³, G. Covone^{14,15,16}, F. Cullen⁸, C. T. Donnan⁸, H. Flores⁶, W. Hartley¹⁷, R. Maiolino^{18,19,20}, R. J. McLure⁸, N. Napolitano^{14,21,22}, M. Paolillo^{14,15,16}, and M. Vaccari^{23,24,25}

(Affiliations can be found after the references)

Received dd mmm yyyy

ABSTRACT

The identification and characterisation of galaxy clusters at different cosmic times are fundamental to constrain cosmological scenarios and to understand the joint evolution of structure formation and galaxies in dense environments. In this work, we analyse the cluster content of the $\sim 4.5 \text{ deg}^2$ XMM-LSS and CDFS VIDEO fields which are expected to be partially covered by the upcoming MOONRISE survey. Using AMICO and WaZP photometric redshift-based cluster finders, we construct a sample of 519 cluster candidates detected by both finders in the redshift range $z = 0.1 - 3$, including 74 detections at $z > 1.5$. For all detections, we identify the Brightest Central Galaxy (BCG) and compute a list of probabilistic cluster memberships. Our photometric redshift measurements of the clusters agree well with spectroscopic redshifts from the literature, when available. From ancillary spectroscopic data, we assign z_{spec} measurements to 116 cluster candidates based on their spectroscopic members and to 204 based on their likely BCGs. We also show that candidates containing Radio-Loud members are efficiently recovered using the prior-based cluster finder PPM. We perform a preliminary analysis of the galaxy content of these candidates, focusing on the Red-Sequence components of their apparent Colour-Magnitude Diagram. By comparing with models of galaxy evolution, we show that this population is consistent with a model of passive evolution with a formation at high redshift, and is already in place at $z = 1.5 - 2.0$. Finally, our cluster sample is used to evaluate how these clusters would be detected and characterised, according to various MOONRISE strategies. We show that cluster spectroscopic confirmation and characterisation could be efficiently achieved up to $z \sim 1.7$ even with the shallowest survey strategy. This open unprecedented insight into the physical properties of high-redshift galaxy clusters and into galaxy formation in dense environments.

Key words. Galaxy clusters, galaxy evolution, photometric survey, spectroscopic survey

1. Introduction

Galaxy clusters are the most massive gravitationally bound and virialised structures in the Universe. They are excellent tracers of the matter density in the cosmic web, providing precious insight into cosmological models. Moreover, they are natural laboratories for studying how galaxies evolve within dense environments over cosmic times. Consequently, systematic studies of these structures over a wide redshift range provide valuable insight into the processes shaping structure formation and into how these processes have impacted galaxy evolution throughout cosmic history.

Studies at low redshift have demonstrated that galaxy cluster environments exert a strong influence on galaxy properties relative to field environments. Several mechanisms are suggested to explain this effect: the hot intracluster medium strips infalling galaxies of their cool gas components as they enter the densest regions of clusters (ram-pressure stripping, Gunn & Gott 1972), repeated high-speed encounters harass low mass galaxies (Li et al. 2012) while major merging within infalling groups shapes and pre-processes the galaxies (Dressler et al. 1997, van Dokkum et al. 1999). As a result, galaxies in clusters tend to be redder and more quiescent, and, as opposed to the field,

mainly presenting themselves as lenticulars and ellipticals. The large fraction of passive galaxies present in cluster cores at low and intermediate redshifts populates a well-defined "Red Sequence" in the Colour-Magnitude diagram (Lidman et al. 2004, 2008, López-Cruz et al. 2004, Mei et al. 2009). The slope and scatter of this relation, as well as its evolution with redshift, have been widely used to constrain models of galaxy formation and evolution (Bower et al. 1992, De Lucia et al. 2007, Kodama et al. 2007, Stott et al. 2009, Valentini et al. 2011).

However, at redshift higher than 1, consensus is not yet achieved. Several analyses show strong star formation in cluster cores (Stanford et al. 2012, Brodwin et al. 2013, Wang et al. 2017). In contrast, some clusters appear to be dominated by red/quiescent galaxies (e.g. Kubo et al. 2021, Andreon et al. 2014, Strazzullo et al. 2019, Noordeh et al. 2021), even in clusters (or protoclusters) at redshift $z \sim 2$ (Kodama et al. 2007, Willis et al. 2020, McConachie et al. 2022). Moreover, some of them already exhibit an in-place or nearly-formed brightest cluster galaxy (BCG) beyond $z = 1$ (e.g. Chu et al. 2021, Shi et al. 2023). Some also show the presence of an intra-cluster light component detected up to $z \sim 2$ (Joo & Jee 2023, Werner et al. 2023), suggesting the complex history of their galaxy populations. The lack of large and representative samples of clusters beyond $z = 1$ currently limits our ability to place strong con-

* e-mail: pierre.galois@oca.eu

straints on the various scenarios of galaxy formation and transformation, and on the efficiency of the associated processes.

Galaxy clusters can be detected in different ways. For example, they can be traced via the X-ray emission of their ionised gas components (e.g. Pacaud et al. 2016, Bulbul et al. 2024), with millimetre observations via the Sunyaev-Zel'dovich effect (e.g. Bleem et al. 2015, Planck Collaboration et al. 2016), through their weak-lensing signal (e.g. Miyazaki et al. 2002, 2007, Gavazzi & Soucail 2007, Oguri & Takahashi 2022, Leroy et al. 2023), or by the direct identification of galaxy overdensities. For the latter, different techniques have been used. They can be based on various cluster features used to limit projection effects, such as, for instance, the identification of red-sequence galaxies (Gladders & Yee 2000, Rykoff et al. 2014). These approaches have been shown to be highly effective at redshifts below 1, where the red sequence is well established, but they may fail to detect higher redshift clusters that lack a prominent red sequence.

With the advent of multi-band photometric surveys, an alternative technique is to detect overdensities of galaxies in photometric redshift space, independent of any prior assumptions on the galaxy population. To be effective, this approach requires high-quality photometric redshifts to minimise contamination from projection effects, especially for the identification of low-mass systems. This led to a multitude of group and cluster catalogues built from a number of surveys: Adami et al. 2010 from Canada-France-Hawaii Telescope Legacy Survey (CFHTLS), Oguri et al. 2018 from Hyper Suprime-Camera (HSC) Subaru Strategic Program, Thongkham et al. 2024 from The Massive and Distant Clusters of WISE Survey 2 (MaDCoWS2), Maturi et al. 2019, 2025 from the Kilo-Degree Survey (KiDS), Aguena et al. 2021 and Benoist et al. 2025 from Dark energy Survey (DES), Doubrawa et al. 2024 from the Javalambre-Physics of the Accelerating Universe Astrophysical Survey (J-PAS). In parallel, groups and clusters catalogues have also been obtained from spectroscopic surveys (for example, the Sloan Digital Sky Survey, SDSS: Miller et al. 2005; Yang et al. 2007; Tempel et al. 2012 and the Galaxy And Mass Assembly, GAMA: Robotham et al. 2011) or with a combined approach based on both photometric and spectroscopic redshifts (for example, the Observations of Redshift Evolution in Large-Scale Environments survey, ORELSE: Hung et al. 2020).

These large-scale photometric and spectroscopic surveys revealed thousands of clusters up to $z = 1$, allowing a deep understanding of cluster properties in the past 7 Gyr of the history of the Universe. However, they lack the depth required to extensively identify and study clusters beyond $z = 1 - 1.5$. Consequently, research for high-redshift clusters is still limited to individual follow-up cases or within deep but small fields, constructed for this purpose. One of these fields is the COSMOS field, which has been widely studied at different wavelengths, allowing the identification of groups and clusters of galaxies over a very large range of redshifts (e.g. Finoguenov et al. 2007, Epinat et al. 2024, Toni et al. 2024, 2025a). However, the relatively small covered area ($\sim 2 \text{ deg}^2$) restricts its statistical power to systems of lower mass, preventing general conclusions to be drawn about the properties of clusters and their evolution over time. The landscape is set to change in the near future with the advent of wide-field, deep optical and infrared surveys such as the Euclid Deep and Wide Surveys (Euclid Collaboration: Mellier et al. 2025, Euclid Collaboration: Scaramella et al. 2022. See Euclid Collaboration: Bhargava et al. 2025 for cluster detection in the Euclid Q1 release).

On the other side, next-generation wide-field, high-multiplex spectrographs (WEAVE, 4MOST, PSF, MOONS) are also expected to transform our understanding of galaxy clusters and their role within the cosmic web. In particular, the MOONS instrument (Cirasuolo et al. 2020) offers a remarkable combination of large multiplexing capability, high sensitivity, and broad simultaneous spectral coverage (spanning from the optical to near-infrared bands), over a wide field. The Main MOONS GTO Extragalactic Survey (MOONRISE, Maiolino et al. 2020) will obtain key spectroscopic information for ~ 500000 galaxies in the redshift range $[0.8, 2.6]$. Its spectroscopic capabilities will be used to get a full three-dimensional characterisation of the galaxy distribution over ~ 11 Gyr, to understand the assembly history of galaxy clusters and their connection to the cosmic web, and test how environment affects the properties of their members galaxies.

The VIDEO XMM-LSS and CDFS fields (Jarvis et al. 2013) are, along the COSMOS field and the Euclid Q1 fields (Euclid Collaboration: Aussel et al. 2025), among the deepest extragalactic fields currently available, with a wealth of available photometric and spectroscopic data up to $z = 1$ and beyond. In this paper, we discuss the high redshift cluster content of these two fields obtained by using two different photometric redshift-based detection algorithms. From the two sets of detections, we build a robust joint sample of cluster candidates in the redshift range $0.1 - 3$. We achieve a first validation of some of these cluster candidates using ancillary spectroscopic data and by comparing with spectroscopically confirmed clusters from the literature. Then, we perform a preliminary analysis of the properties of the galaxies within these candidates by constructing their apparent Colour-Magnitude diagram, and by comparing with models of galaxy evolution. Finally, these candidates are used as a benchmark to test the capabilities of the MOONRISE survey for cluster science.

This paper is organised as follows. In Sect. 2 we describe the content of the datasets used in this work and explain how they have been constructed. In Sect. 3, we introduce and describe the two cluster finder algorithms used in this work. Section 4 is dedicated to the description of the construction of a subsample of robust detections. Then, in Sect. 5, we perform a first validation of this particular subset of detections using ancillary spectroscopic data and previously confirmed galaxy clusters. In Sect. 6, we focus on the identification of the Red-Sequence components of our candidates within their apparent Colour-Magnitude diagram, and compare with models of galaxy evolution to put constraints on the properties of this particular subpopulation of galaxies. Section 7 is dedicated to testing the ability of the different MOONRISE survey strategies to observe and characterise these systems, and finally, we discuss these results and draw our conclusion in Sect. 8. Throughout this paper, we assume a flat Λ CDM cosmology with $H_0 = 70 \text{ kms}^{-1} \text{ Mpc}^{-1}$, $\Omega_m = 0.30$ and $\Omega_\Lambda = 0.70$. All the quantities in pc correspond to physical lengths.

2. Data

2.1. The VIDEO catalogues of galaxies

As part of the ongoing preparation for the MOONS MOONRISE GTO programme (Cirasuolo et al. 2020; Maiolino et al. 2020), near-infrared selected catalogues spanning the VIDEO XMM-LSS and CDFS footprints have been produced. The details of these catalogues will be provided in future work (McLeod et al., in prep). We will summarise their construction here.

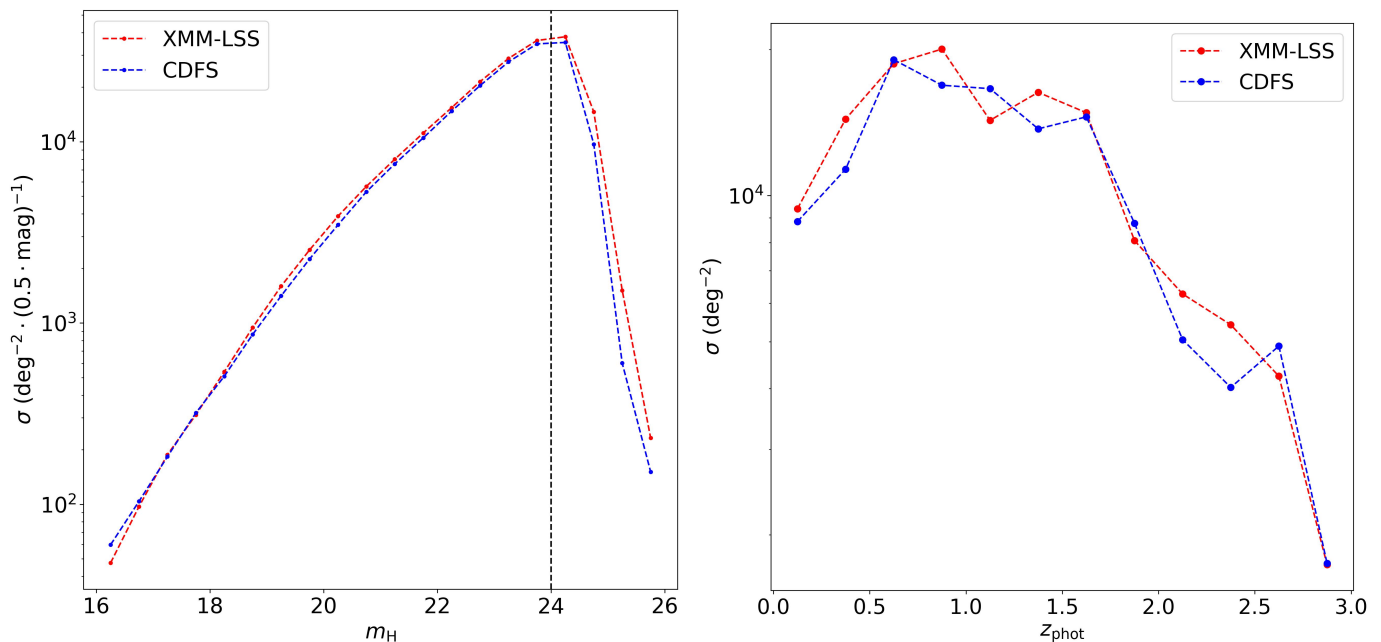


Fig. 1: *Left:* VISTA H-magnitude galaxy counts for the XMM-LSS and CDFS fields. The vertical dashed line represent the $m_H = 24$ completeness limit. *Right:* Distribution of the photometric redshifts of galaxies with $m_H < 24$ in the XMM-LSS and the CDFS within the redshift range $z_{\text{phot}} \in [0, 3]$.

Each of the VIDEO (Jarvis et al. 2013) XMM-LSS and CDFS fields spans approximately $\approx 4.5 \text{ deg}^2$. For both of these fields, McLeod et al. (in prep) uses the available Y, J, H, and K_s imaging from VIDEO DR4. The CDFS photometry includes UV/optical u -, g -, r - and i -band data taken from the VLT Survey Telescope VOICE survey (Vaccari et al. 2016). Available HSC imaging in g -, r -, i - and z -band are also included, although we note that the r -band coverage is available only over a $\approx 2 \text{ deg}^2$ subset of the area (Ni et al. 2019, 2021). Finally, in the mid-infrared, IRAC $3.6\mu\text{m}$ and $4.5\mu\text{m}$ imaging publicly released from the Cosmic Dawn Survey (Euclid Collaboration: Moneti et al. 2022) are included.

The XMM-LSS field consists of three sub-fields with varying UV to mid-infrared coverage. In particular, the UltraDeep Survey (UDS) covering a $\approx 0.8 \text{ deg}^2$ region benefits from significantly deeper coverage in J, H and K from UKIDSS (Lawrence et al. 2007) UDS DR11 (Almaini et al. in prep). UV coverage mainly comes from CFHTLS T0007 (Hudelot et al. 2012) u -band imaging, with additional CFHT MegaCam u -band imaging from MUSUBI (Mehta et al. 2018; Wang et al. 2022) over the UDS footprint. In the optical, the XMM-LSS field is covered by HSC g -, r -, i -, z - and y -band imaging, as well as by HSC narrow-band NB816 and NB921 filters, as part of the second data release from the Subaru Strategic Program (SSP; Aihara et al. 2019). In the XMM3/CFHTLS-D1 sub-field, there is additional CFHT g -, r - i - and z -band imaging from the aforementioned CFHTLS T0007 release (Hudelot et al. 2012), while in XMM1/UDS Subaru SuprimeCam (SSC) imaging in B, V, R, i and z' (Furusawa et al. 2008) have been included. The SSC images used were those prepared as ancillary data products for the UDS DR11 data release by C. Simpson (Gemini). Finally, the more recent z'_{new} imaging with improved red wavelength sensitivity from Furusawa et al. (2016) are used. In the mid-infrared, the XMM-LSS benefits from IRAC $3.6\mu\text{m}$ and $4.5\mu\text{m}$ imaging from the SERVS programme (Mauduit et al. 2012). For the deeper coverage in XMM1/UDS, McLeod et al. (in prep) utilises

the Mehta et al. (2018) release which includes the SPLASH (PI Capak, see Mehta et al. 2018), SERVS (Mauduit et al. 2012), SEDS (Ashby et al. 2013) and S-CANDELS (Ashby et al. 2015) datasets.

Prior to catalogue construction, all imaging was PSF-homogenised to a common Moffat profile of FWHM $0.95''$, with the exception of the CDFS VOICE u , HSC g and HSC r imaging, which were found to have $\text{FWHM} \gtrsim 0.95''$. The catalogue construction follows the methods employed in McLeod et al. 2021. SOURCE-EXTRACTOR (Bertin & Arnouts 1996) was run in dual-image mode, with the VIDEO H-band sets as the detection image. For the XMM1/UDS sub-field, a UKIRT WFCAM H-band catalogue was also produced, in order to leverage the superior depth in that region. Photometry was measured in 2-arcsec diameter apertures, with the exception of the lower resolution IRAC imaging. To measure IRAC photometry, the deconvolution software TPHOT (Merlin et al. 2015) was used. TPHOT takes the positional and surface brightness information for objects from their higher resolution images (i.e. the detection H-band) as an input, along with a transfer kernel between the higher and lower resolution PSFs, in order to fit model fluxes for these same objects in the lower resolution IRAC imaging.

The final working catalogues used in this study are limited to regions that have an optimal coverage at different wavelengths to ensure a better homogeneity of the derived photometric redshifts in the two fields. In particular, some regions not covered neither by the r - or i -bands were excluded. In addition, several series of masks were applied to limit the number of false positive sources or sources with shallow photometry (essentially at the edges). Based on the Gaia DR3 catalogue (GAIA Collaboration 2020), stars were masked by disks with magnitude-dependent radii following an empirical relation. Brightest ($m_r \leq 15$) foreground galaxies were also masked. Finally, several image artefacts that caused the concentration of spurious detections in space and redshift were masked by hand. The resulting effective areas are

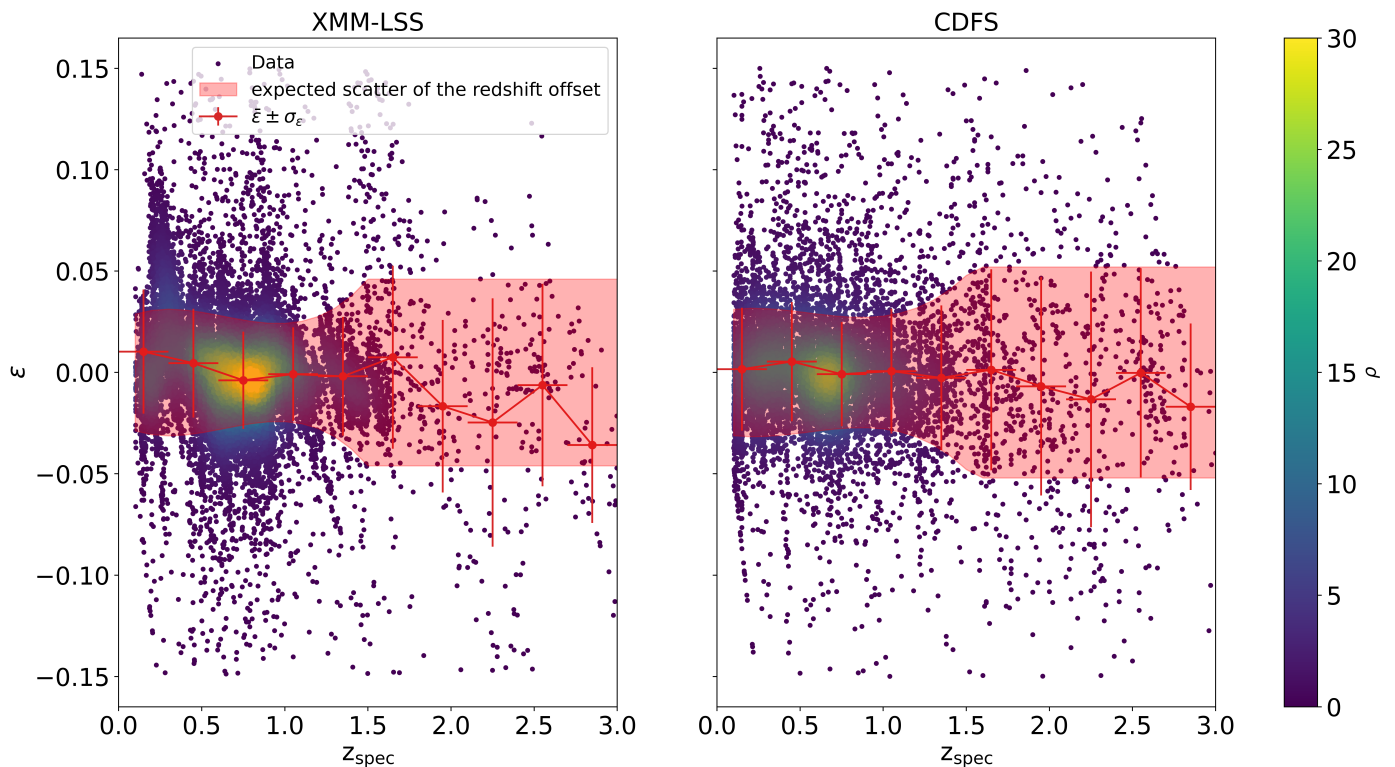


Fig. 2: Evolution of the mean bias $\bar{\varepsilon}$ in bins of z_{spec} in the XMM-LSS (left panel) and the CDFS (right panel). The y-axis error bars represent the standard deviation σ_{ε} computed in the corresponding redshift bin. The x-axis error bars represent the bin widths. All data points are shown in the background, with density reconstructed using a Gaussian kernel. The filled red area represents the estimated scatter of the redshift offset, derived from polynomial fitting of σ_{ε} . We assume it constant beyond $z = 1.5$, due to the lack of available spectroscopic data to extrapolate it properly. The colour maps represent the amplitude of the probability density function of the points distribution.

4.55 deg² for the XMM-LSS field and 4.11 deg² for the CDFS field.

The normalised galaxy number counts in bins of VIDEO H-band magnitude (m_H in the following) are shown in left panel of Fig. 1. They are consistent and show a very similar depth. In the rest of the paper, we only consider galaxies brighter than $m_H = 24$, the magnitude beyond which the two samples become incomplete. At this magnitude, we obtain galaxy densities of 38.0 and 36.1 arcmin⁻² for the XMM-LSS and CDFS fields, respectively.

2.2. The photometric redshifts

Photometric redshifts z_{phot} were determined for sources by taking the median z_{phot} from seven different SED fitting runs. Five of these used the template fitting code LEPHARE (Arnouts & Ilbert 2011), including BC03 (Bruzual & Charlot 2003), three alternate PEGASE2 (Fioc & Rocca-Volmerange 1999) runs utilising different star-formation histories and metallicities, and the COSMOS (Ilbert et al. 2009) SED libraries. The remaining two runs were performed with EAZY (Brammer et al. 2008), using the default PCA templates and the PEGASE2 libraries. Once the median z_{med} of all z_{phot} values returned by these codes was found, the photometric redshift was fixed to this value.

In the following, we will only consider galaxies within the redshift range $z_{\text{phot}} \in [0, 3]$. The right panel of Fig. 1 shows the redshift distribution of galaxies in the redshift range $[0, 3]$. Overall, galaxies appear to be distributed in redshift in a similar way in both fields.

2.3. The spectroscopic redshifts

In addition to the photometric redshift catalogues, we have access to catalogues of spectroscopic redshifts (z_{spec}) for both fields, compiled from various public surveys. Spectroscopic information is associated to the photometric catalogues within a 1 arcsec radius, resulting in 28292 matches in the XMM-LSS and 12367 in the CDFS. For this matching, only highly reliable spectroscopic redshifts were considered, based on the quality flags provided by each survey. Table 1 and Table 2 list the different surveys used in this study and the associated number of unique counterparts for the XMM-LSS and CDFS galaxies within the photometric redshift range $z = 0.1 - 3$. The available spectroscopic data allow us to sample well large domains of magnitude and redshifts. However, as we show in Fig. A.1, some domains remain poorly covered, especially at redshifts beyond 1.5 or at magnitudes $m_H \gtrsim 23$. Our capacity to evaluate the quality of photometric redshifts in these domains will therefore be limited.

2.4. Quality assessment of the photometric redshift

To quantify the quality of photometric redshifts, we compute the deviation of z_{phot} relative to z_{spec} measurements for the same galaxy by introducing the offset ε defined as:

$$\varepsilon = \frac{z_{\text{phot}} - z_{\text{spec}}}{1 + z_{\text{spec}}}. \quad (1)$$

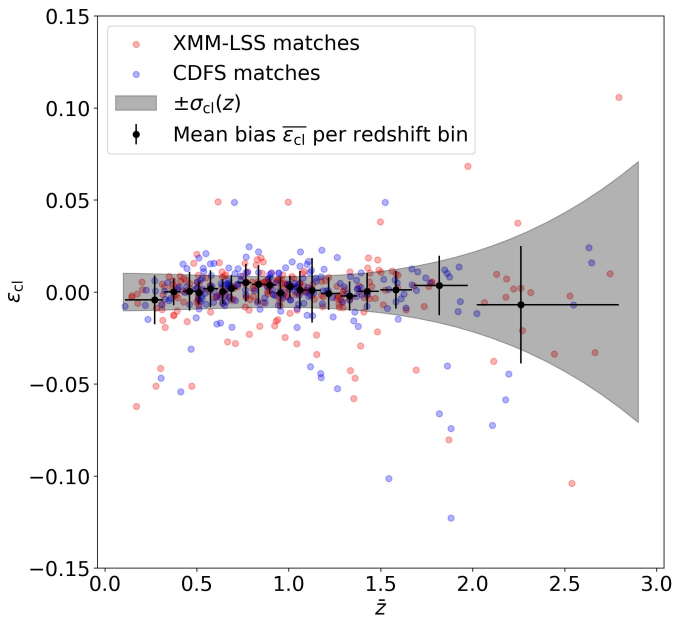


Fig. 3: Evolution of the redshift scatter ε_{cl} between the AMICO and WaZP matched detections for a projected physical separation criterion of $R = 150$ kpc. The black dots represent the mean bias computed per bins of redshift, with the associated bins width and standard deviation as x and y-error bars, respectively. The gray envelopes represent the estimated dispersion $\sigma_{cl}(z)$ of the offset between the AMICO and WaZP z_{phot} for a pair of detections at a given redshift. We limit the plot to the y-range $[-0.15, +0.15]$ for the purpose of readability, 5 matches from the CDFS and 4 from the XMM-LSS are outside this range. The last bin is larger than the others to take into account the lower density of points at these redshifts.

In this work, we use z_{spec} as the reference measurement of galaxy redshifts, with errors considered negligible compared to those from z_{phot} . Following Ilbert et al. 2006, $\sim 5\%$ of the galaxies with $|\varepsilon| > 0.15$ are considered as catastrophic errors. The remaining 95% of galaxies are shown in Fig. 2. They are used to estimate the mean bias, $\bar{\varepsilon}$, and the associated standard deviation, σ_{ε} , computed in bins of z_{spec} .

Up to $z \sim 1.5$, statistics remain well controlled, with a mean bias amplitude smaller than 0.01 and a maximal scatter of $\sigma_{\varepsilon}(z) \sim 0.03$ in both fields. However, at higher redshift, because of the lack of spectroscopic data, z_{phot} metrics cannot be accurately estimated. We derive the scatter $\sigma_{\varepsilon}(z)$ in the range $z = 0.1 - 1.5$ in both fields via a polynomial fit, and assume the scatter to be constant beyond this upper limit, as we cannot constrain it properly at these redshifts. These are shown as the red envelopes in Fig. 2. These functions will be used in the following to estimate the error on the galaxy photometric redshift at a given redshift for the corresponding field when needed.

3. Detection of galaxy clusters

In this section, we describe the two cluster finders used in this work: AMICO and WaZP. Both algorithms have been widely used over the last few years, proving themselves highly efficient at identifying cluster and group candidates over a wide range of redshift (e.g., see Maturi et al. 2019, 2023, 2025, Toni et al. 2025a, Euclid Collaboration: Bhargava et al. 2025 for AMICO, Aguena et al. 2021, Benoist et al. 2025 for WaZP).

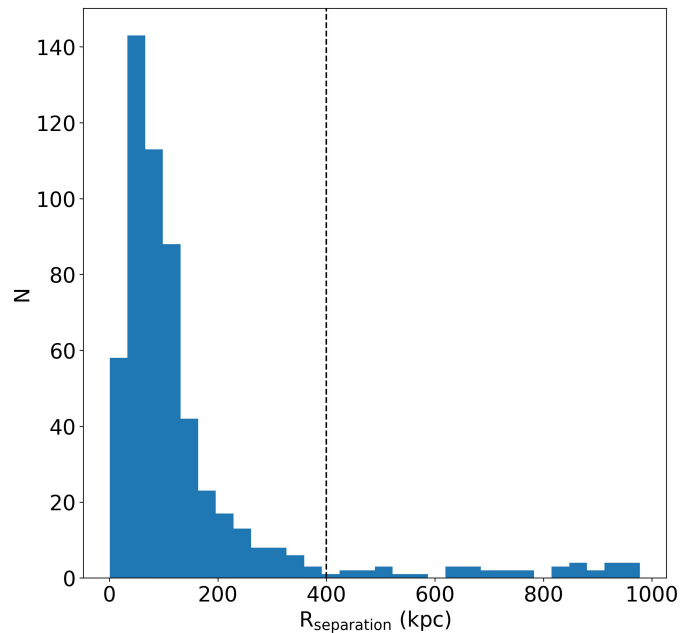


Fig. 4: Angular separation distribution of the AMICO-WaZP pairs of detections for a $R = 1.0$ Mpc matching radius at the $2\sigma(z)$ level. The vast majority of the distribution is contained within $R = 200$ kpc ($\sim 83\%$), with a few pairs separated by more than 400 kpc ($\sim 7\%$ of the pairs, in both fields). The dashed vertical line represent the 400 kpc matching criterion we derived from this figure.

Both cluster finders weight galaxies depending on their magnitudes relative to a reference magnitude that varies with redshift. The goal is to build a cluster richness estimator that would provide the same richness to a cluster that would be seen at different redshifts. This reference magnitude is chosen here to be the expected knee of the Luminosity Function, $m^*(z)$. To trace its evolution, we compute the flux variation of a passively evolving population formed in a single burst at high redshift and calibrated with known clusters at low redshift (e.g., Lin et al. 2006). In this study, we derive $m_H^*(z)$ from the passive evolution of a burst galaxy with a formation redshift $z_{form} = 5$ taken from the PEGASE2 library (burst_sc86_zo.sed, Fioc & Rocca-Volmerange 1997).

3.1. AMICO

The Adaptive Match Identifier of Clustered Objects (AMICO, Bellagamba et al. 2018; Maturi et al. 2019) is designed to detect galaxy clusters in photometric catalogues using the linear optimal matched-filter technique described in Maturi et al. 2005. In this framework, the data are modelled as $D(x) = S(x) + N(x)$ where the cluster signal is given by $S(x) = A \cdot M_c(\mathbf{x})$. Here, A is the cluster amplitude and M_c is a model describing the observable properties of clusters members, \mathbf{x} , which in this case include right ascension, declination, photometric redshift with its associated uncertainty, and H-band magnitude. The amplitude, A , which scales with cluster richness, is obtained through the convolution of the data with an optimal filter, as detailed in Bellagamba et al. 2018; Maturi et al. 2019. The noise term, N , captures the contribution of noise measured directly from the data.

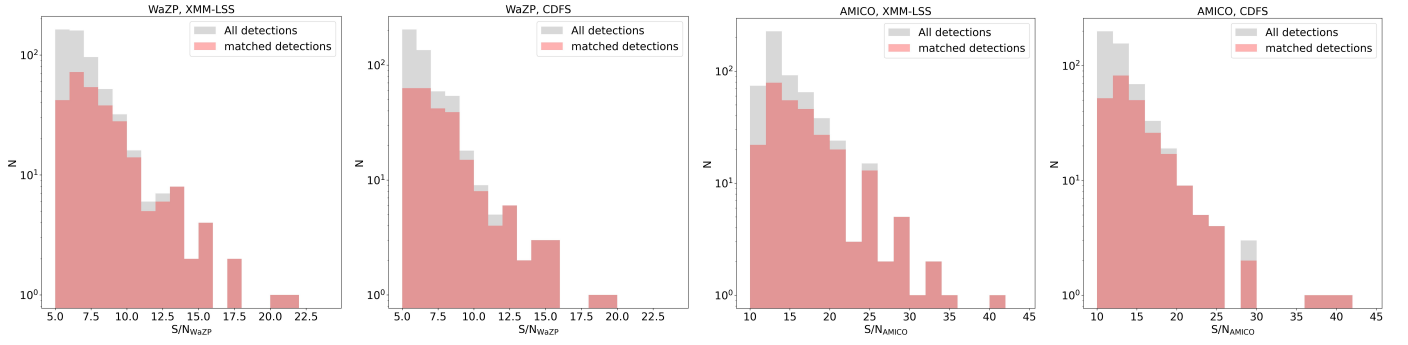


Fig. 5: Distribution of the AMICO and WaZP S/N of the matched cluster candidates compared to all the detections in the XMM-LSS and CDFS.

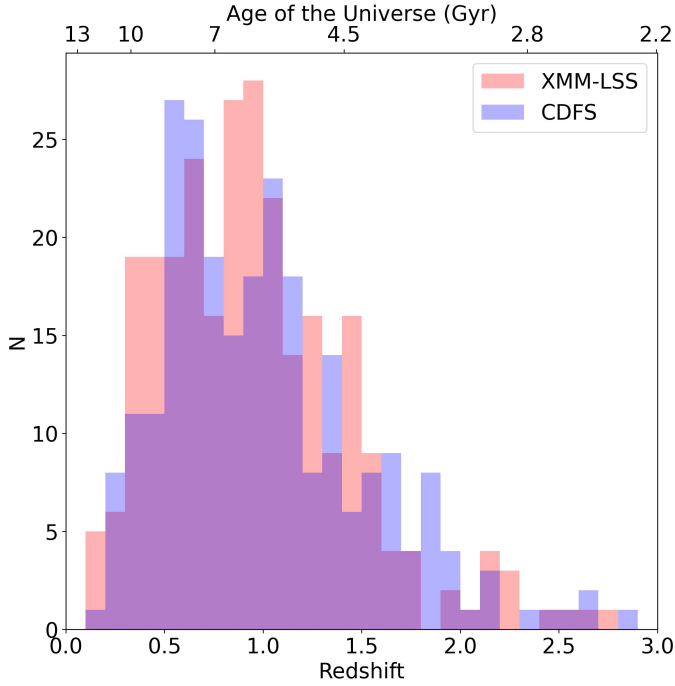


Fig. 6: Distribution of the photometric redshifts of the AMICO-WaZP joint cluster candidates in the XMM-LSS (red) and CDFS (blue). These distributions appear similar in both fields.

The filtering kernel is automatically derived via a constrained minimisation procedure, producing an unbiased minimum-variance estimate of the cluster amplitude A . AMICO scans the sky with an angular and redshift resolution of 0.3 arcmin and 0.01, respectively, and iteratively identifies the cluster candidates by locating the most significant signal-to-noise peaks produced by the filter. The scheme is used iteratively to allow for better identification of blended detections.

The probability of the i -th galaxy being a member of the j -th detection is estimated as

$$P_i(j) = P_{f,i} \frac{A_j M_{c,j}(r_{ij}, m_i) p_i(z_j)}{A_j M_{c,j}(r_{ij}, m_i) + N(m_i, z_j)} \quad (2)$$

Here, r_{ij} is the angular separation between detection and galaxy, and $P_{f,i} = 1 - \sum_k P_i(k)$ is the probability of the i -th galaxy to belong to the field. These quantities are defined iteratively during the detection process starting with $P_{f,i} = 1$. The intrinsic richness of the j -th detection is defined as $\lambda_{*j} = \sum_i P_i(j)$, where the

Table 1: List of spectroscopic surveys and number of z_{spec} used for the XMM-LSS galaxies.

Survey name	Number of galaxies	Reference
DESI-DR1	10399	DESI Collaboration et al. (2025)
GAMA-DR3	2158	Baldry et al. (2018)
SDSS-DR16	2652	Ahumada et al. (2020)
UDSz	1330	Bradshaw et al. (2013) McLure et al. (2013)
VIPERS-PDR2	11753	Scoddeggio et al. (2018)

Table 2: List of spectroscopic surveys and number of z_{spec} used for the CDFS galaxies.

Survey name	Number of galaxies	Reference
2dF	185	Colless et al. (2001)
2dFLenS	23	Mortlock et al. (2001)
3DHST	3724	Brammer et al. (2012) Momcheva et al. (2016)
ACES	3730	Cooper et al. (2012)
ATLAS	367	Mao et al. (2012)
OzDES	3271	Lidman et al. (2020)
ELG-FIGS	63	Pharo et al. (2020)
MUSE-Wide	671	Urrutia et al. (2019)
VANDELS	93	Pentericci et al. (2018)
VUDS	45	Tasca et al. (2017)
VVDS	195	Le Fèvre et al. (2005)

sum runs over all galaxies within R_{200} (i.e. the radius of a sphere of mean density equal to 200 times the critical density of the Universe) of the template cluster model and magnitudes smaller than $m_* + 1.5$ evaluated at the detection redshift.

3.2. WaZP

The Wavelet Z-Photometric (WaZP) cluster finder (Aguena et al. 2021, Benoist et al. 2025) is designed for the optical detection

of galaxy clusters from multi-wavelength photometric imaging galaxy surveys. It is based on the search for projected overdensities of galaxies in photometric redshift space. It does not make any assumption about the existence of a Red-Sequence and relies only weakly on the cluster radial profile and on the luminosity function (redshift-dependent faintest magnitude). A complete description of the WaZP detection method is presented in Aguena et al. 2021 and Benoist et al. 2025. Here, we provide a summary of the main steps.

Overdensity peaks are initially extracted from pixelised wavelet-based density maps constructed from the galaxy catalogue in various photometric redshift slices. In each slice, galaxies are weighted based on their redshift probability distribution function (here, Gaussian). Then, the peaks of successive slices are merged and the peak with the largest S/N enters the final list of clusters. The accuracy of the cluster position on the sky is limited by the resolution of the wavelet maps chosen here as $1/16$ Mpc.

Then, following the prescription of Castignani & Benoist (2016), cluster membership probabilities are computed. They depend on galaxy cluster-centric distances, magnitudes, and photometric redshifts. Finally, cluster members are used to jointly estimate the cluster richness and radius. The richness is the sum of the membership probabilities within a radius that corresponds to an overdensity of 200 times the mean number density of the galaxy background (similar to Hansen et al. 2005). Here, for the richness computation, only members brighter than $m^*(z_{\text{cluster}}) + 1.5$ are considered.

4. Building of a AMICO-WaZP joint cluster sample

From the raw lists of AMICO and WaZP detections, we aim to construct a sample of robust cluster candidates, identified by both cluster finders. Although they both rely on the same photometric redshifts, as they adopt very different assumptions, galaxies are combined in different ways, based on different selection criteria and weights. Thus, the overdensities identified by both algorithms are less likely to be spurious detections.

To cross-match the two samples, we consider a subset of highest S/N detections, ensuring an equal cluster density between the two cluster finders. While high S/N cuts lead to higher purities, lowering the S/N threshold improves completeness. To maximise purity while achieving sufficient completeness at high redshift, a good compromise is reached for an initial detection density of 120 deg^{-2} in both fields. This choice is justified by the comparison to galaxy mock catalogues performed in the context of the Euclid survey with H-band depth and photometric redshift uncertainties similar to the VIDEO fields studied here. From the first panel of fig. 8 of Euclid Collaboration: Adam et al. 2019, a density of 120 deg^{-2} cluster detections between redshifts 0 and 2 leads to purity levels between 85 % and 90 % for WaZP and AMICO. Therefore, we expect our joint catalogue to reach a high level of purity. In addition to this statistical argument, a careful visual inspection of the entire joint sample is performed below. A cluster density of 120 deg^{-2} is achieved with the following S/N thresholds:

- In the XMM-LSS:
 - $S/N \geq 5.4$ for WaZP
 - $S/N \geq 11.5$ for AMICO
- In the CDFS:
 - $S/N \geq 5.2$ for WaZP
 - $S/N \geq 10.7$ for AMICO

which correspond initially to 550 and 500 AMICO and WaZP detections in the XMM-LSS and the CDFS, respectively. Note that the different absolute values of S/N are due to the different S/N definitions used by the two algorithms.

The WaZP-AMICO cross-match is performed with the publicly available Python library CLEvaR (<https://github.com/LSSTDESC/CLEvaR>). The adopted strategy is a two-way cylindrical matching within a given physical radius and redshift offset length. The two cluster lists are first ranked by decreasing order of S/N. Matched clusters are removed from the list. If a cluster has more than one possible counterpart, the one with the highest S/N is selected. The two matching parameters are empirically determined in two steps to minimise random associations.

We first match detections based only on their angular separation with a very small maximum offset of 150 kpc and examine in Fig. 3 the resulting redshift offset distribution, $\varepsilon_{\text{cl}} = (z_{\text{AMICO}} - z_{\text{WaZP}})/(1 + \bar{z})$, where \bar{z} is the mean redshift of each pair. Taking into account the typical photometric redshift errors, more than 98% of the matches can be considered as physical pairs (i.e. with $\Delta z/(1 + z) < 0.15$). The mean and standard deviation as a function of the redshift are estimated with the biweight estimator (Beers et al. 1990). We find essentially no relative redshift bias between the two cluster finders up to $z \sim 1.7$ in both fields. The mean scatter of the redshift offsets is $\overline{\sigma}_{\text{cl}} \sim 0.01$. Its redshift dependence, $\sigma_{\text{cl}}(z)$, is modelled as a third-order polynomial, shown as a gray envelope in Fig. 3.

To estimate the optimal matching radius, we perform a second matching, selecting pairs with a redshift offset within $\pm 2\sigma_{\text{cl}}(z)(1 + z)$ and with a maximum angular separation of $R = 1.0$ Mpc. The resulting angular separation distributions are shown in Fig. 4, where more than 90% of the pairs are separated by less than 400 kpc. Based on this, we define our optimal matching radius to be $R = 400$ kpc. For the matching parameters we derived, knowing the initial density of detection, the probability to have random association between the two cluster finders is estimated to be lower than 1%.

Using the parameters previously defined, the matching leads to 277 and 250 pairs of detections in the XMM-LSS and CDFS, respectively, which correspond to $\sim 50\%$ of both samples. A large fraction of the unmatched systems would have a counterpart, but at a S/N lower than the adopted thresholds.

Figure 5 shows the S/N distribution of the matched and unmatched detections for the two cluster finders. In general, the higher the S/N, the higher the matching rate. There are a few exceptions at high S/N but these can be explained by the scatter between the S/N of the two algorithms, or by pairs with centring or redshift offsets just outside our matching window.

A systematic visual inspection of the entire sample was performed. Only very few cases appeared problematic. We identified respectively 6 and 2 spurious detections in the XMM-LSS and CDFS due to insufficient masking around foreground bright sources or observation artefacts. These were removed from the following analysis. In a few cases it was also noticed the presence of nearby masked regions that could potentially impact the centring or other measured characteristics associated to the detections. To take this into account, we compute for each candidate the fraction of area within a 1.0 Mpc disk centred at the cluster position that is effectively covered by unmasked data around.

Our final working cluster catalogue is therefore composed of 271 and 248 cluster candidates in the XMM-LSS and CDFS, respectively. In particular, 31 (XMM-LSS) and 43 (CDFS) detections are found at redshifts beyond 1.5. The redshift and spatial distribution of the joint AMICO-WaZP detections are shown in

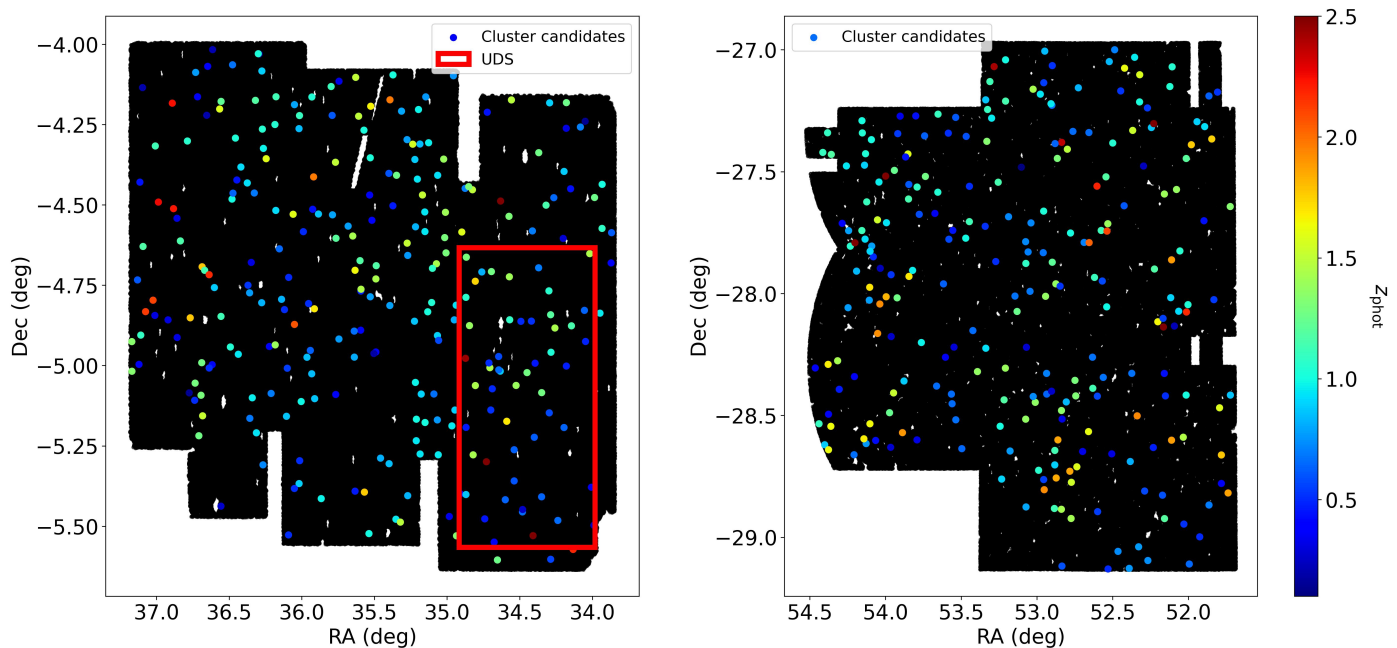


Fig. 7: Spatial distribution of the cluster candidates within the XMM-LSS (left) and the CDFS (right). The black backgrounds represent the footprints of both fields. The colours indicate the mean photometric redshift of the AMICO-WaZP joint detections. The red rectangle marks the limit of the footprint of the UDS subfield, the region which will be covered by MOONRISE in the XMM-LSS.

Fig. 6 and Fig. 7, respectively. These latter show a homogeneous coverage over the two footprints, with no suspicious overdensities in redshift or space. We represent in Fig. 7 the limit of the UDS footprint by a red rectangle. This is the region which will be covered by the MOONRISE survey in the XMM-LSS (see Sect.7 for more details). Finally, in Fig. 8, we show six examples of high S/N cluster candidates at $z_{\text{phot, joint}} \sim 1 - 1.6$ and four examples of high S/N cluster candidates at $z_{\text{phot, joint}} \sim 2$ in Fig. 9. They all present a significant concentration of galaxies. All of them are in the domain of redshift which will be covered by MOONRISE, showing good examples of the kind of systems that could be identified by MOONS.

In the following, each detection of the joint sample is assigned a new centring, RA_{joint} and $\text{Dec}_{\text{joint}}$, and a new redshift, $z_{\text{phot, joint}}$, defined as the average of the centrings and redshifts provided by each cluster finder. The joint sample detections are labelled with the prefix "Cl", while their WaZP and AMICO identifiers are labelled, respectively, with the prefixes "W" and "A". In this study, the membership probabilities that are used are coming by default from the WaZP algorithm, except when stated explicitly. Extracts of the XMM-LSS and CDFS catalogues can be found in Table B.1 and B.2 in Appendix B. For each candidate we provide its ID (Col. 1), its joint RA-Dec coordinates (Col. 2-3), its joint z_{phot} (Col. 4), its WaZP and AMICO richnesses (Col. 5-6) and S/N (Col. 7-8). If exists, its spectroscopic redshift estimation, and the number of members used to compute it are shown in Col. 9-10 (see Sect. 5.2 for more details). If exists, the spectroscopic redshift derived from its BCG is shown in Col.11 (see Sect.5.1 and Sect.5.2 for more details). Finally, the coverage fraction is shown in Col. 12.

5. Analysis of the joint WaZP-AMICO sample

5.1. Identification of brightest cluster galaxies

For all cluster candidates, we aim to identify their likely brightest cluster galaxies (BCGs). As BCGs are generally found very close to the centre of their parent clusters, we identify, for each cluster, the brightest member (in m_{H}) within 400 kpc from the centre as a likely BCG candidate, here referred to as the brightest central member (BCM). If we consider the global brightest cluster members, these are included within 400 kpc for $\sim 65\%$ of the cluster candidates. For those beyond 400 kpc, they are likely to be outliers, with a median membership probability of ~ 0.3 . In addition, the median difference between the m_{H} of the BCM and of the brightest cluster member is ~ 0.33 , with a BCM among the top three brightest members in $\sim 91\%$ of the cases. Thus, in order to avoid contamination from potential outliers and as BCGs are expected to be close to the centre of their parent clusters, except in cases of massive merging events, it appears reasonable to choose the BCMs as the most likely BCG candidates.

Comparison with memberships from AMICO shows similar results, where the BCG candidates we identified are mostly in common with the WaZP one, except for a few cases caused by differences in terms of membership computation or angular separation between the different cluster centroids.

5.2. Spectroscopic redshift estimation.

In this section, we use our compilation of spectroscopic redshifts, described in Sect. 2.3, to estimate the spectroscopic redshifts of the cluster detections when such data are available. We first use the spectroscopic redshift distribution of the identified member galaxies to infer the cluster redshift. The main difficulty, particularly at high redshift where several concentrations may appear in the spectroscopic redshift distribution, is to iden-

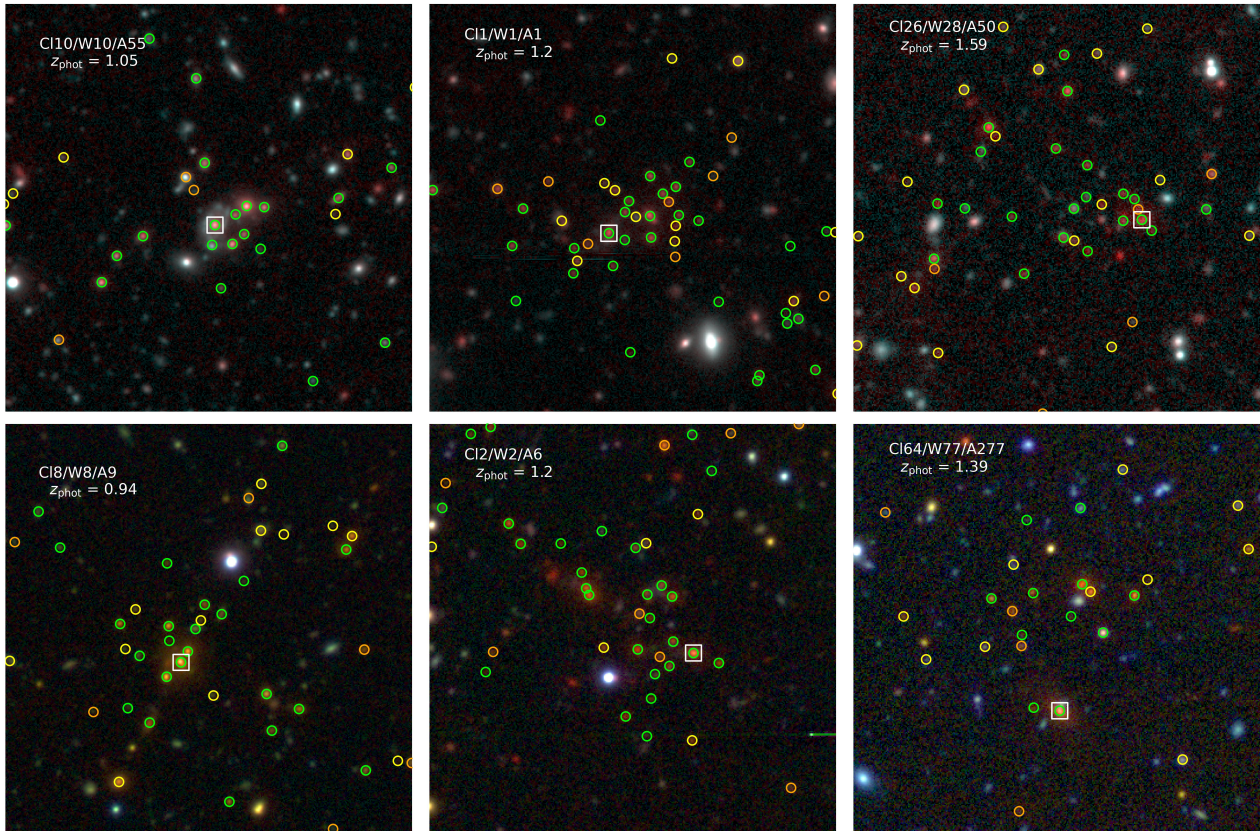


Fig. 8: Coloured cutouts of three XMM-LSS (top) and three CDFS (bottom) cluster candidates from the joint catalogue in the redshift range $z_{\text{phot, joint}} \sim 1 - 1.6$. All images are built using HSC R, I, and VIDEO H bands. The field of view is $0.6 \times 0.6 \text{ Mpc}^2$. We display the position of the members with membership probabilities of 0.75-1.0, 0.5-0.75 and 0.25-0.5 by green, yellow and orange circles, respectively. The location of the BCG candidate is represented by a white square (see Sect.5.1). The images are centred at the joint cluster position. The full membership extends beyond the FoV.

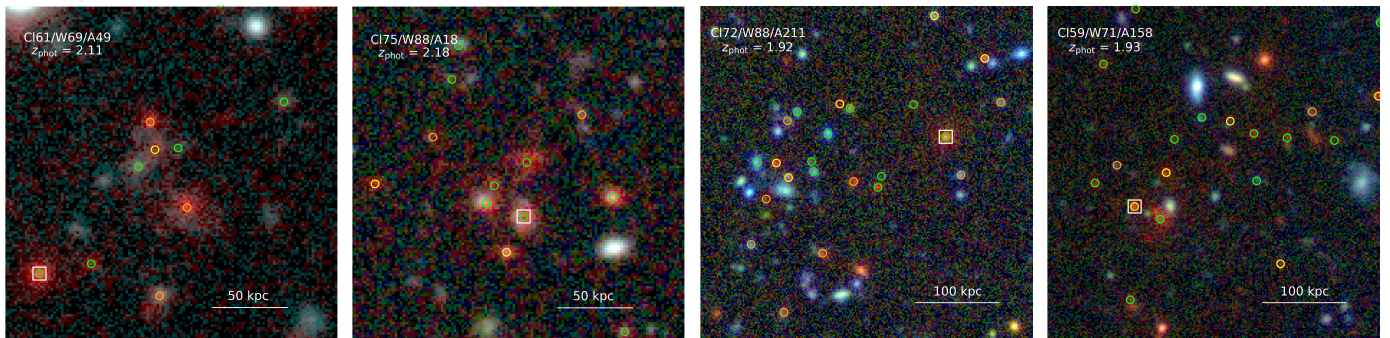


Fig. 9: Same as Fig.8 but for two XMM-LSS (left) and two CDFS (right) cluster candidates from the joint catalogue at $z_{\text{phot, joint}} \sim 2$. The FoV was adapted for each candidate to avoid perturbation of the image dynamic by bright foreground sources. The physical scale is indicated by the white line on the bottom of each image.

tify which one corresponds to the detection made by the cluster finder in photometric redshift space. To mitigate this issue, we restrict the analysis to galaxies identified as members and limit it to a cylindrical region centred on the coordinates of the cluster detection with a radius of 1 Mpc, and with an initial spectroscopic window $|(z_{\text{spec}} - z_{\text{DET}})/(1 + z_{\text{DET}})| \leq 0.15$, where z_{DET} is the photometric redshift of the cluster detection. Focussing on the inner region of the cluster helps minimise outlier contamination in the outskirts of the cluster. The use of a large initial redshift-space window is intended to account for the bias and scatter previously observed between photometric and spectro-

scopic redshifts. We convolve the z_{spec} distribution with a Gaussian kernel of bandwidth $0.005(1 + z_{\text{DET}})$ and identify the main concentration in the smoothed z_{spec} distribution. The large value for the bandwidth (corresponding to the velocity dispersion of a rich cluster) has been chosen in order to erase peaks in the distribution caused by small clumps along the line of sight. We then select a rest-frame window of $3000 \text{ km} \cdot \text{s}^{-1}$ around the main concentration and estimate the cluster redshift $z_{\text{spec, gaussian}}$ using the location bi-weight estimator from Beers et al. 1990, shown to be robust to non-Gaussian underlying populations (thus to in-

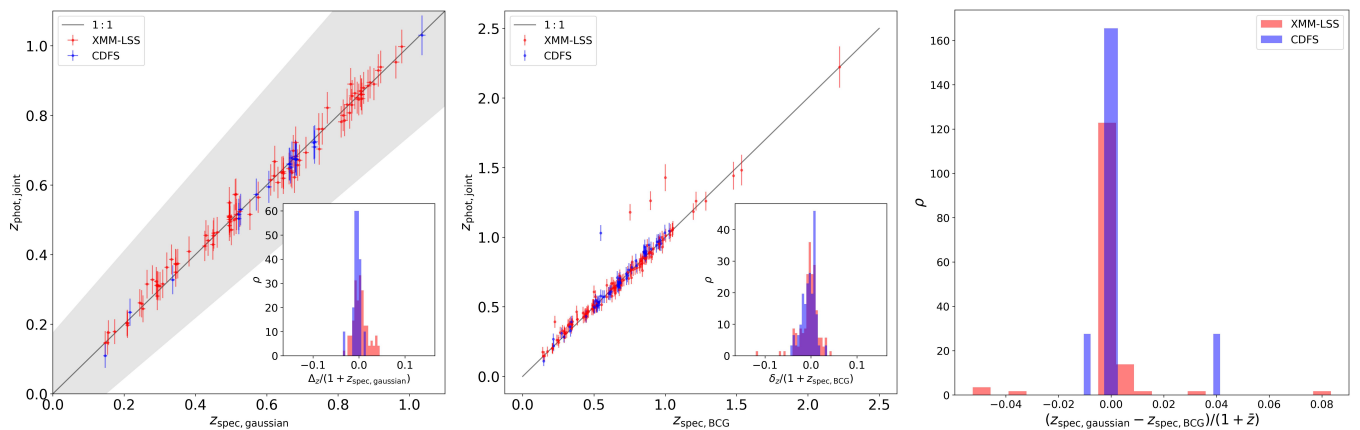


Fig. 10: *Left:* Relation between $z_{\text{phot, joint}}$ and the estimated $z_{\text{spec, Gaussian}}$. The x-axis error bars are derived using a Gaussian kernel bandwidth, while the y-axis error bars are derived from the galaxies photometric redshift metrics (1σ confidence level). The inset panel shows the probability distribution function of the offset $(z_{\text{phot, joint}} - z_{\text{spec, Gaussian}})/(1 + z_{\text{spec, Gaussian}})$ between the two redshift measurements. The gray area represents the $|(z_{\text{spec}} - z_{\text{phot}})/(1 + z_{\text{phot}})| < 0.15$ selection window. *Middle:* Relation between $z_{\text{phot, joint}}$ and $z_{\text{spec, BCG}}$. The y-axis error bars are derived from the galaxies photometric redshift metrics (1σ confidence level). The inset panel shows the probability distribution function of the offset $(z_{\text{phot, joint}} - z_{\text{spec, BCG}})/(1 + z_{\text{spec, BCG}})$ between the two redshift measurements. *Right:* Distribution of the scatter between the z_{spec} estimation from statistics over the members and the one derived from the BCG candidates for the 99 cluster candidates with both measurements available.

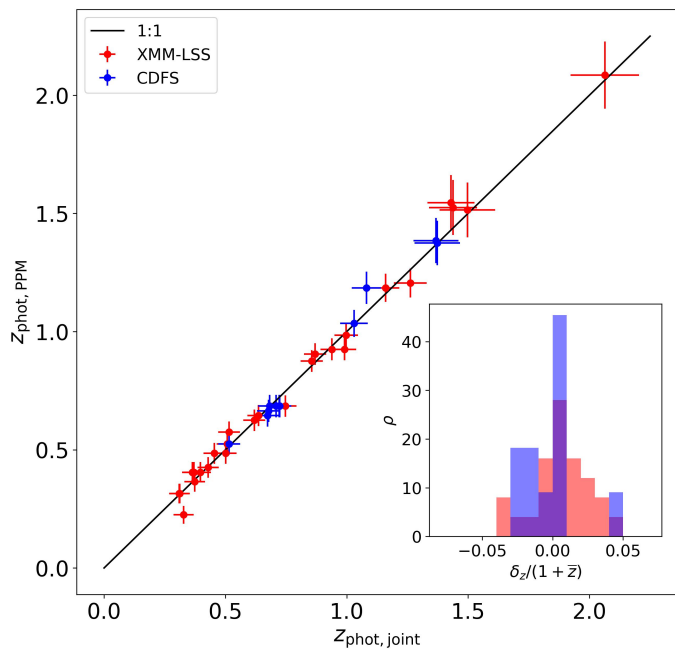


Fig. 11: Relation between the redshift of PPM overdensities and cluster candidates for the associated pairs in the XMM-LSS (red) and CDFS (blue). The inset panel shows the probability distribution function of the offset $(z_{\text{phot, PPM}} - z_{\text{phot, joint}})/(1 + \bar{z})$. We observe an overall good agreement between the redshifts of the matched candidates.

terloper contamination). Only measurements with more than five members are kept in the following analysis.

Following this process, we estimate spectroscopic redshift measurements for 96 and 20 cluster candidates in the XMM-LSS and the CDFS, respectively. The left panel of Fig. 10 shows the $z_{\text{spec, gaussian}} - z_{\text{phot, joint}}$ relation for these 116 cluster candidates, together with the 1:1 relation. The mean scatter of the points over the entire redshift range with respect to the 1:1 relation is

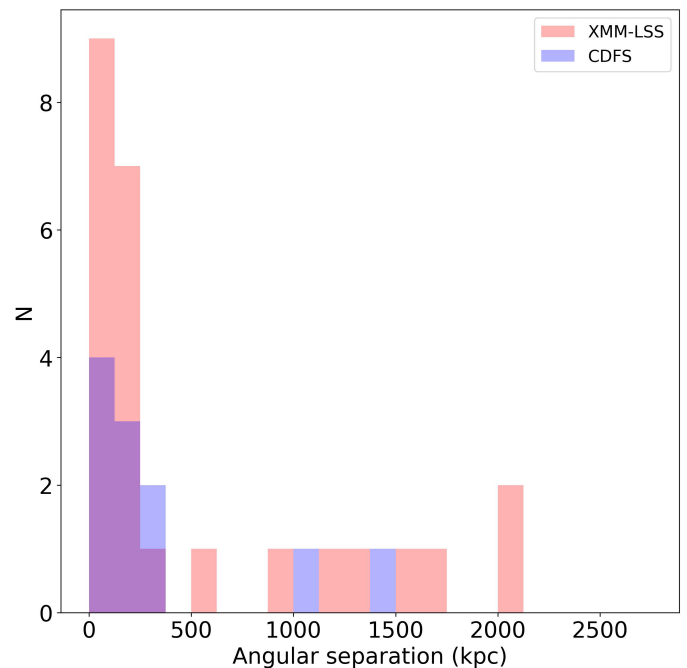


Fig. 12: Distribution of the angular separation between the cluster candidates and their associated PPM overdensities. We used the WaZP cluster centre definition here, as the matching is based on the WaZP membership.

estimated to be ~ 0.01 – 0.02 , indicating a good overall agreement between the spectroscopic and photometric redshift estimates.

As a second approach to estimate the spectroscopic redshift of our cluster candidates, we use the spectroscopic redshift of the BCGs candidate when available. Among the BCG candidates we identified previously, 204 have z_{spec} measurements. The central panel of Fig. 10 shows the relation between the BCGs z_{spec} and the $z_{\text{phot, joint}}$ of their parent clusters. First, the four outliers above the 1:1 relation correspond to galaxies with catas-

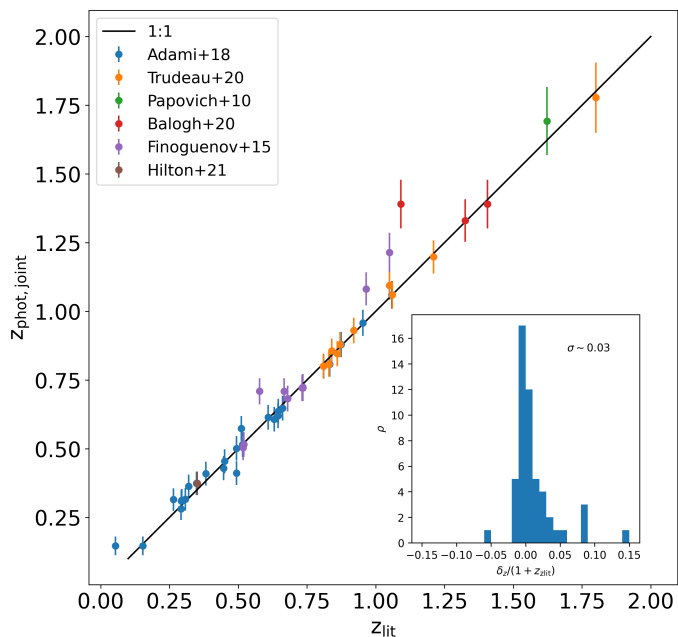


Fig. 13: Relation between the spectroscopic redshift from the literature, z_{lit} , and the mean AMICO-WaZP redshift, $z_{\text{phot, joint}}$, for candidates that match with the ancillary cluster catalogues. The inset panel shows the distribution of the offset $(z_{\text{phot, joint}} - z_{\text{lit}})/(1 + z_{\text{lit}})$. The error bars are derived from the galaxies photometric redshift metrics, at 1σ level. The standard deviation of the relation is approximately $\sigma \sim 0.03$, highlighting good agreements between our results and those from the literatures.

trophic photometric redshifts. The inset histogram shows the distribution of the offset $(z_{\text{phot, joint}} - z_{\text{spec, Gaussian}})/(1 + z_{\text{spec, Gaussian}})$ between the joint photometric redshift and the BCGs spectroscopic ones, without the 4 catastrophic cases. The standard deviation of the $(z_{\text{phot, joint}} - z_{\text{spec, BCG}})/(1 + z_{\text{spec, BCG}})$ distribution is comparable to the one for cluster spectroscopic redshift estimation with a Gaussian kernel, with $\sigma \sim 0.02$ in both fields. There are 85 and 14 cluster candidates with z_{spec} estimation from both BCGs and statistics over memberships in the XMM-LSS and the CDFS, respectively. The right panel of Fig. 10 shows the distribution of $(z_{\text{spec, Gaussian}} - z_{\text{spec, BCG}})/(1 + \bar{z})$, with $\bar{z} = (z_{\text{spec, Gaussian}} + z_{\text{spec, BCG}})/2$. The standard deviation of the relationship between these two estimators of clusters z_{spec} is ~ 0.001 , showing the general very good agreement that we have between these two estimators. We have 8 cluster candidates where the offset between the $z_{\text{spec, BCG}}$ and the $z_{\text{spec, Gaussian}}$ is larger than 0.01. For these galaxies, their photometric redshift measurements are all compatible with their spectroscopic ones. However, compared to the photometric redshift of their parent clusters, their z_{phot} is slightly shifted, with offsets between 0.01 and 0.06, in absolute values. We conclude that these galaxies may possibly be foreground/background objects, and so could be less likely BCGs candidates.

5.3. Search for overdensities around radio sources

Instead of systematic, blind, searches for cluster candidates, another approach is to search for overdensities around some subclasses of galaxies which are often considered as signposts of galaxy clusters and galaxy overdensities in general, such as radio emitting galaxies (e.g. Wylezalek et al. 2013, Castignani et al.

2014b), or sub-millimetre galaxies (e.g. Calvi et al. 2023). In this paper, we apply the well established Poisson probability method (PPM) around cluster candidates members identified as radio emitting sources. The PPM searches for megaparsec-scale overdensities of galaxies around a given target. Through the use of a solid positional prior and an accurate photometric redshift sampling, PPM partially overcomes the limitations deriving from low number-count statistics and shot-noise fluctuations, which are particularly relevant in the high- z Universe, such as in the case of proto-clusters. More specifically, the PPM method uses photometric redshifts of galaxies to search for overdensities around each target along the line of sight. To search for overdensities around a sample of radio sources, the PPM adopts an accurate sampling of the photometric redshift information to the detriment of a less sophisticated tessellation of the projected space, which is performed in terms of concentric annuli centred around each target. We refer to previous studies for a detailed description of the method (Castignani et al. 2014a,b), its wavelet-based extension (Castignani et al. 2019), and the applications (Castignani et al. 2014b, 2019; Calvi et al. 2023).

Here, we used VLA radio sources from Kellermann et al. 2008 for the CDFS and from the VLA FIRST survey (Becker et al. 1995) for the XMM-LSS. Each radio source was associated with its optical counterpart within our catalogue with a 2 arcseconds separation criterion and using its photometric redshift, we computed the 1.4 GHz rest-frame luminosity using:

$$L_{1.4\text{GHz}} = 4\pi F_{1.4\text{GHz}} \cdot D_L(z_{\text{phot}})^2 \cdot (1 + z_{\text{phot}})^{\alpha-1} \quad (3)$$

with D_L the luminosity distance and α the radio spectral index. Here, we used $\alpha = 0.8$, according to Chiaberge et al. 2009. To homogenise both catalogues of radio sources, we consider only sources with $L_{1.4\text{GHz}} > 10^{23.2} \text{ W}\cdot\text{Hz}^{-1}$. This selection allows us to safely exclude star forming galaxies, which typically have lower radio luminosity densities. Higher values such as those considered in this work are instead typically associated with radio loud active galactic nuclei, including radio galaxies and radio-loud quasars.

Following this criterion, we identified 213 and 158 radio sources in the XMM-LSS and the CDFS, respectively. Since the footprint of the radio survey only covers a fraction of the CDFS, we only consider cluster candidates which are at least partially covered by the footprint of the radio catalogue. We identified 27 and 11 cluster candidates containing, at least, one radio source in the XMM-LSS and the CDFS, respectively. Using PPM, we searched for galaxy overdensities around these sources. For clusters with several radio-loud members, we identified the main PPM counterpart as the closest to the cluster centre. We identified a PPM counterpart for 26 XMM-LSS and 11 CDFS cluster candidates. Among them, there are 2 XMM-LSS and 1 CDFS pairs of cluster candidates that share common PPM detections, as their associated radio sources are common members. Figure 11 shows the relation between the redshift of the cluster candidates and the ones of their associated PPM overdensities. We have overall good agreement in terms of redshift between them, with an offset lower than 0.05 in absolute value. Figure 12 shows the distribution of the angular separation between the cluster candidates and their associated PPM overdensities. Cases with an angular separation larger than 1.0 Mpc represent $\sim 27\%$ and $\sim 18\%$ of the entire set of pairs in the XMM-LSS and CDFS, respectively, and could be seen as less likely associations. On the other hand, as PPM is designed to search for overdensities of galaxies on Mpc scale, these cases could also correspond to clusters embedded within larger structures. Spectroscopic follow-

ups at the Mpc scale are required to better understand these cases (which will be one of the purposes of MOONRISE).

Altogether, 37 of the 38 AMICO-WaZP cluster candidates containing a radio source are also detected by PPM. Except for a few cases, we obtain very good redshift and angular separation agreement. Overall, as these candidates are also well identified by a third, independent cluster finder, the PPM analysis strengthens the robustness of these joint AMICO-WaZP detections.

5.4. Comparison with ancillary cluster catalogues

Following the work described above, we compare our sample of cluster candidates to spectroscopically confirmed, multi- λ , clusters available in the literature. For this purpose, we used 49 XXL clusters from Adami et al. 2018, 10 from Trudeau et al. 2020, 6 GOGREEN/GCLASS clusters from Balogh et al. 2020, one Spitzer-selected high redshift cluster from Papovich et al. 2010, one ACT-DR5 cluster from Hilton et al. 2021 and 29 ECDFS groups from Finoguenov et al. 2015.

We cross-matched our cluster candidates with the ancillary data using a maximal radius criterion of $R = 1.0$ Mpc and $\delta z/(1+z) < 0.15$. If we have several matches with our list of candidates, we consider only the one with the highest WaZP S/N. Following this process, we found a counterpart for 27 clusters from Adami et al. 2018, for all clusters from Trudeau et al. 2020, for 3 GOGREEN/GCLASS clusters, 10 ECDFS clusters, one for the cluster from Papovich et al. 2010 and one for the ACT cluster (the candidate with the highest WAZP/AMICO S/N). Except for a few cases, clusters from the literature are always recovered by at least one of the cluster finders. However, due to the matching criteria used to build the AMICO-WaZP joint sample, some of them were excluded during the process and appear as unmatched when compared to our final list of cluster candidates.

Figure 13 shows the comparison between the redshifts of the cluster candidates and those of their counterparts in the literature. Overall, a good agreement is found, except for a few outliers. The standard deviation of the offset $(z_{\text{phot, joint}} - z_{\text{lit}})/(1 + z_{\text{lit}})$ is approximately 0.03. We have 4 cluster candidates for which we measure an offset of 0.06 or more, representing a deviation larger than $\pm 2\sigma_z$. One of them matches with a GOGREEN/GCLASS cluster, one with Adami et al. 2018 clusters and two with ECDFS clusters. All of these cases could possibly be due to random associations with foreground low-mass groups of galaxies, induced by the large redshift criterion we use here. We refer to Appendix C for a detailed description of them.

Table 3: Filters selection as a function of cluster redshifts $z_{\text{phot, joint}}$ for the construction of the CMD described in Sect. 6.

Redshift range	color	magnitude
0.1 – 0.4	<i>g-r</i>	<i>r</i>
0.4 – 0.7	<i>r-i</i>	<i>i</i>
0.7 – 1.1	<i>i-z</i>	<i>z</i>
1.1 – 1.4	<i>z-Y</i>	<i>Y</i>
1.4 – 1.7	<i>Y-J</i>	<i>J</i>
1.7 – 2.3	<i>J-H</i>	<i>H</i>

Notes. Lowercase italic letters are for the HSC filters, while capital letters are for the VISTA ones.

6. Colour-magnitude relation.

In this section, we analyse the Colour-Magnitude diagrams (CMDs) in apparent magnitudes of the cluster candidates previously selected. We aim to test for the presence of a passive, red population of galaxies in the inner parts of these clusters in the different redshift bins probed. Indeed, many studies have shown the presence of passive galaxies at the centre of rich clusters organised as a ridge-line in the CMD, the so-called Red-Sequence (RS), widely observed at low and intermediate redshifts (see e.g. López-Cruz et al. 2004). However, despite some evidence of the existence of a RS up to $z \sim 2$, a consensus is not yet achieved for $z > 1$.

For each cluster, the CMD is built considering only members within 0.5 Mpc from the cluster centre, and brighter than $m_{\text{bright}} + 1.5$. Here, m_{bright} is defined as the brightest galaxy (in the reddest band of the CMD) as a function of redshift in the entire galaxy sample. In practice, to avoid outliers, we compute the median magnitude of the 95% brightest galaxies per redshift bin. In order to optimally frame the 4000 Å break, we adopt the redshift-dependent filter selections described in Table 3. The analysis is interrupted at $z_{\text{phot, joint}} = 2.3$ as the Balmer break cannot be bracketed any more with the available filters. As some regions are not covered by the four HSC filters, in the first four redshift bins, the analysis is limited to clusters that are covered by the relevant filters at least at a 50% level within a radius of 1.0 Mpc. In the end, we are left with 461 candidates.

In Fig. 14 are shown examples of CMDs for clusters at different redshifts. They display a bimodal distribution, with a blue component and a more or less pronounced redder ridge-line. To measure the mean colour of the red ridge-line, the distribution of colours is modelled as a two-components Gaussian mixture. We estimate the mean colour μ_r of the ridge and its scatter σ_r by identifying the red Gaussian component. We consider the estimation of the mean colour as valid if we have more than 3 members in the colour range $\mu_r \pm \sigma_r$. Applying this criterion, 11 cases are rejected. After visual inspection of each CMD, we identify 16 additional cases where the red ridge is either too poorly populated or not sufficiently prominent to be fitted reliably. The excluded cases typically correspond to candidates that are very poor or systems at high-redshift, where a well-established RS is not expected to be systematically present. For the other candidates, the bi-Gaussian successfully isolates the red ridge-line, yielding a mean normalised scatter $\sigma_r/(1+z) \sim 0.05$ mag, consistent with the results of similar studies at lower redshifts (e.g. Andreon 2003, Jaffé et al. 2011).

We compare the mean colour of the red component with predictions from models of galaxy evolution. To model colours of a typical quiescent galaxy population, we follow the prescription from Andreon et al. 2006, assuming a high-redshift formation over a relatively short timescale, followed by purely passive evolution. For this purpose, we use the CIGALE SED fitting code (Boquien et al. 2019) and compare the resulting mean colours with those measured for our cluster candidates. We model an exponentially declining star formation history (sfh2exp module) with a formation redshift at $z_f = 10$ and assume a folding timescale of the main stellar population of $\tau_{\text{main}} = 0.75$ Gyr. We use a single stellar population derived from the Bruzual & Charlot 2003 model (bc03 module), computed for different metallicities: $Z = 0.004, 0.008, 0.02$ and 0.05 . Here, a Chabrier 2003 initial mass function (IMF) is used.

Figure 15 shows the evolution of the mean colour of the red component as a function of the redshift of the AMICO-WaZP joint cluster candidates. We represent by open circles the 16

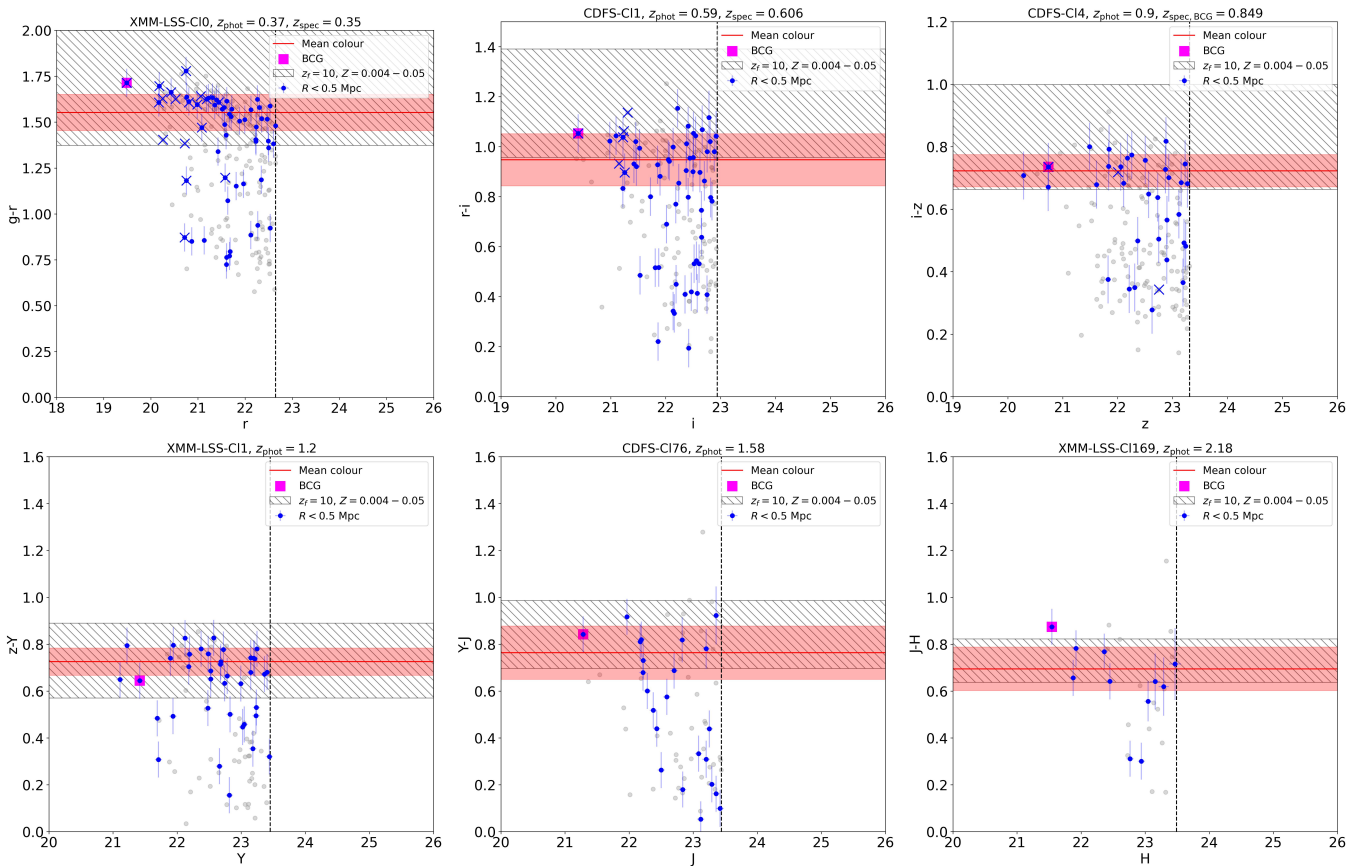


Fig. 14: Examples of Colour-magnitude diagrams (CMDs) for candidates at different redshifts. Each example corresponds to one combination of filters, as described in Table 3. The grey points represent all members, while the blue ones represent the members selected within 0.5 Mpc. The red line and the envelope represent the mean colour of the red ridge and its associated standard deviation derived in Sect. 6. The vertical dashed black line represents the applied magnitude cut. We compare the mean colour to a model of galaxy evolution (grey dashed region) with a redshift of formation at $z_f = 10$, for the range of metallicity $Z = 0.004 - 0.05$. We refer to Sect. 6 for more details. For candidates with spectroscopic redshift estimation computed in Sect. 5.2, we indicate by a blue cross members within $R = 1.0$ Mpc and within a window of $\Delta v = \pm 3000 \text{ km} \cdot \text{s}^{-1}$ around the cluster's z_{spec} . If the spectroscopic redshift estimation is derived from the BCG, we specify it in the title of the panel.

cases we rejected following the visual inspection. For the remaining 434 candidates, we observe an overall good agreement between the model predictions and the mean colour of the red component measured for the candidates. This suggests the presence of a population of quiescent galaxies already in place at $z \sim 2$, as reported by previous studies (e.g. Kodama et al. 2007, Andreon et al. 2014, Cerulo et al. 2016, Strazzullo et al. 2019, Willis et al. 2020, Toni et al. 2025b). We also observe a few systems in the last bin of redshifts that are redder than the predictions of the model used here. Nevertheless, we find that by slightly reducing the folding timescale to 0.5 Gyr, we can reproduce the mean colours of these candidates. This may indicate the presence of a more massive population of galaxies, as suggested by De Lucia et al. 2006. In any case, spectroscopic follow-ups are required to better understand the galaxy population within our candidates, since they might have different evolutionary histories depending on the mass or evolutionary stage of their parent clusters.

Comparisons with AMICO memberships return similar results, with the presence of a population of red galaxies already in place at $z \sim 2$, compatible with a scenario of high-redshift formation and passive evolution.

7. Probing the galaxy population of clusters with MOONRISE

In the previous sections, we have demonstrated the potential of applying state-of-the-art cluster-finding algorithms to deep, multi-band photometric VIDEO fields for which high-quality photometric redshifts have been derived. By cross-matching the detections obtained with the two cluster finders, using an optimised S/N threshold for both codes, we constructed a joint cluster-candidate catalogue that reaches redshift 2 with good purity ($> 80\%$ based on numerical simulations).

Part of the analysed VIDEO fields (XMM-LSS and CDFS) is expected to be covered in spectroscopy in the near future by MOONRISE. We hereafter investigate how many spectroscopic redshift members would be confirmed by MOONRISE in cluster candidates previously identified in those fields using photometric redshifts. MOONRISE observational strategies are currently being defined within the consortium, in order to meet the broad scientific objectives. In this section, we illustrate, using real data, how the group and cluster populations detected in the VIDEO fields are expected to be sampled under these different strategies.

We focus here on two observational strategies designed to optimally trace the effects of environment on galaxy evolution (the Medium-Deep strategy) and the evolution of large-scale

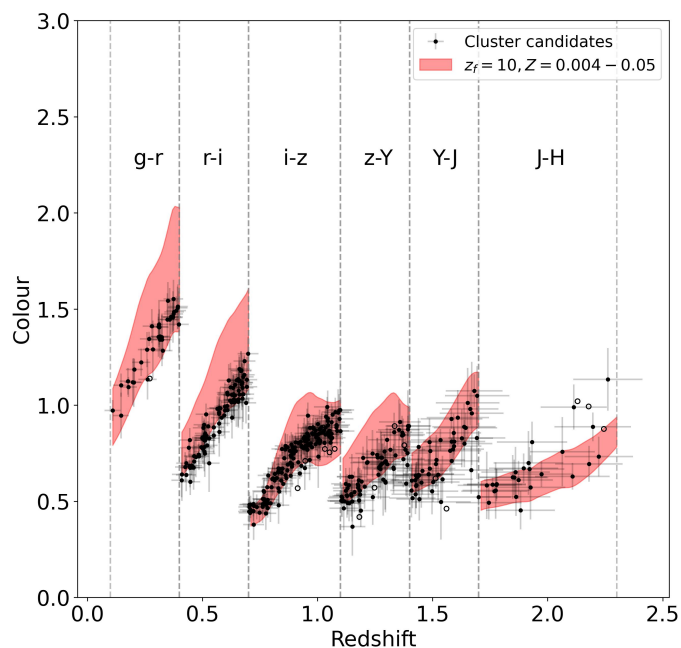


Fig. 15: Evolution of the apparent mean colour of the Red-Sequence for the AMICO-WaZP joint candidates as a function of redshift. The coloured envelopes represent the expected colours derived from models within the metallicity range $Z \in [0.004, 0.05]$ for a formation redshift at $z_f = 10$, for a folding time of $\tau_f = 0.75$ Gyr, without any subsequent burst of star formation. The error bars for the x-axis represent the error on the photometric redshift estimated in Sect. 2.4. Open circles represent the 16 cases that were rejected after visual inspection, for which the Red-Sequence was too poor to be correctly identified. The limits of the different redshift ranges associated with each set of filters are represented as dashed lines.

- For the Medium-Deep: $m_H < 24$ for star-forming galaxies, $m_H < 23$ for passive galaxies
- For the Shallow-Wide: $m_H < 23$ for star-forming galaxies, $m_H < 22$ for passive galaxies

To mimic these observing strategies and assess their impact on the sampling of the cluster population, we applied the corresponding galaxy selections to the members of the joint cluster candidates and estimated the expected recovery rate as a function of redshift. We used the U-V-J rest frame colour-colour diagram shown in Fig. 16 to separate passive and star-forming galaxies. They are considered as quiescent if their rest frame U, V and J rest-frame magnitudes follow the relation:

$$\begin{cases} U - V > 0.88 \times (V - J) + 0.49 \\ U - V > 1.3 \end{cases} \quad (4)$$

for $z \in [0.8, 2.0]$, and

$$\begin{cases} U - V > 0.88 \times (V - J) + 0.42 \\ U - V > 1.1 \end{cases} \quad (5)$$

for $z \in [2.0, 2.3]$.

We made use of rest-frame magnitudes and physical parameters provided by BAGPIPES spectral modelling and fitting tool (Carnall et al. 2018, Carnall et al. 2019), with models redshift fixed at the z_{phot} of each galaxy (see Sect. 2.2). The code uses the 2016 updated version of Bruzual & Charlot 2003 as a stellar population model, based on a Kroupa 2001 IMF. A Calzetti et al. 2000 dust attenuation law was used, with allowed reddening A_V between 0 and 4.

In order to maximise statistics, we use the full XMM-LSS and CDFS fields to test the Shallow-Wide strategy. For the Medium-Deep strategy, we focus, as an example, on the deepest region covered by the UDS to meet the depth requirements. In this case, because of the limited field size, our results may be affected by cosmic variance. We divide the redshift range into three bins: $[0.8, 1.2]$, $[1.2, 1.7]$ and $[2.0, 2.3]$. For each strategy, we adopt the assumption of a uniform random selection of galaxies with an overall completeness of 70% across the entire field for the given strategy, without accounting for fibre positions. We first apply the observational strategy criterion to the full catalogue and then randomly select 70% of the galaxies, repeating this procedure 100 times. Within each redshift bin, we then compute the total number of member galaxies recovered per cluster, as well as their distribution in magnitude bins. These quantities are weighted by the cluster membership probabilities. Finally, we average over the one hundred realisations to estimate the mean number of members recovered per cluster for a given strategy.

Figures 17 and 18 show the mean weighted number of recovered members per bins of H magnitude per cluster for the XMM-LSS+CDFS under the Shallow-Wide strategy, and for the UDS under the Medium-Deep strategy, respectively. These figures clearly indicate that the Shallow-Wide Strategy will be key for massive redshift confirmation of clusters candidates (264 on the whole region, corresponding to $\sim 30 \text{ deg}^{-2}$) over the redshift range $[0.8-1.7]$ with more than 15 members per cluster. The Medium-Deep strategy yields a higher number of members per cluster (on average ~ 30) thereby enabling detailed kinematic studies and cluster mass measurements through velocity dispersions for a comparable density of detections ($\sim 24 \text{ deg}^{-2}$). It is worth noting also the good balance achieved between passive

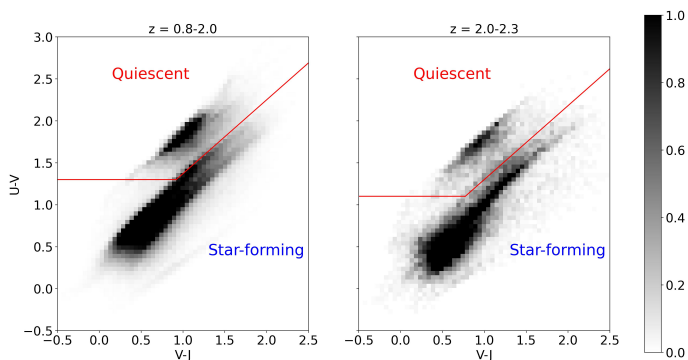


Fig. 16: Stacked UVJ diagram of galaxies with $z_{\text{phot}} \in [0.8 - 2.0]$ (left) and $z_{\text{phot}} \in [2.0 - 2.3]$. The red line represents the limit between quiescent and star-forming galaxies empirically derived, as defined by Eqs. 4 and 5.

structure (the Shallow-Wide strategy). To meet scientific objectives, observational requirements in terms of redshift coverage, magnitude limits, and sampling rate were derived from mock catalogues simulating the properties of the VIDEO fields (De Lucia et al. 2007). The resulting goals are as follows: a survey completeness of 70%, redshift coverage of $z = 0.8 - 1.7$ and $z = 2.0 - 2.3$, with different limiting magnitudes for each observational strategy:

and star-forming sampling, thanks to the use of different magnitude selection criteria for each population. At higher redshifts ($z > 2$), we enter the regime of rare systems. In this case, spectroscopic confirmation appears barely achievable for only 12 candidates in the XMM-LSS+CDFS fields with the Shallow-Wide strategy, corresponding to a projected density of $\sim 1 \text{ deg}^{-2}$. The Medium-Deep strategy could not be tested in this redshift range but may be investigated in the future using other existing deep surveys (i.e. COSMOS).

We would like to emphasise the caveats of this approach. First, to better control purity and ensure a robust analysis, we decided to consider only high S/N detections in common for both algorithms, which strongly limits the number of detections. Second, we cannot exclude the possibility that a small fraction of objects suffers from line-of-sight contamination. Estimating this fraction accurately would require a detailed characterisation of the selection function on the data, which is beyond the scope of this paper. However, given the use of the joint approach and a conservative S/N threshold, this fraction is expected to remain well below 20%. Despite these limitations, the analysis presented in this section demonstrates that the Shallow-Wide and Medium-Deep strategies, defined using mock catalogues, appear very promising when applied on real data and complement each other very effectively in the characterisation of galaxy populations in dense environments. MOONRISE will be instrumental in validating these systems and thus unambiguously characterising the selection function of groups and clusters up to redshift 2.

8. Discussions and conclusion

We presented a catalogue of 519 cluster candidates in the redshift range [0.1, 3], jointly detected by the WaZP and AMICO cluster finders in the XMM-LSS and CDFS VIDEO fields. Selecting only the common detections from the two cluster finders results in a catalogue of cluster candidates with enhanced purity, but it may exclude potentially valid detections identified by only one of the two methods, making this a very conservative choice.

Comparisons with spectroscopically confirmed clusters from the literature and the various estimations of spectroscopic redshift measurement for eligible cluster candidates show, overall, good agreement with the estimated photometric redshift. We showed that cluster candidates containing radio-loud galaxies can be efficiently identified by the PPM algorithm, a third, different cluster finder.

For each cluster candidate, we provide a list of likely members, which were used to address the evolution of galaxy properties through redshift. The study of the apparent Colour-Magnitude diagram of each individual cluster candidate allows the identification of a Red-Sequence-like component up to $z \sim 2$. Comparison with models of galaxy evolution highlights the presence of a population of red, ancient galaxies already in place at $z \sim 2$. These results are consistent with previous studies, reinforcing the hypothesis that the galaxy populations within clusters has undergone a peak in their transformation process at $z \sim 2-3$, leading to the population we observe at lower redshift.

All these results tend to reinforce our confidence about the true nature of these candidates and lead to preliminary insights into the properties of galaxies within clusters at $z > 1$. Due to our method of selection and the limited surface of both fields, our conclusions are limited to this specific subpopulation, and further work is needed to determine the selection function and assess the representativeness of the cluster catalogue. We also plan to investigate the properties of these candidates in greater

detail in future studies. This will include their stellar mass function and the characteristics of their galaxy populations.

Spectroscopic follow-ups of these candidates will be essential to confirm their redshifts and physical properties. While targeted follow-ups can be performed for a limited number of clusters, a comprehensive three-dimensional mapping from a large-scale spectroscopic survey is necessary to enable systematic redshift confirmation and to assess line-of-sight contamination. Indeed, massive spectroscopy has proven to be essential for understanding the selection function of optical cluster catalogues, as demonstrated by the use of DESI spectroscopy to characterise RedMapper cluster catalogues (Myles et al. 2025). MOONRISE will allow us to go a step further in redshift and to characterise the selection function up to redshift of 2. It will open a new window on cluster formation in the redshift range [0.8, 2.3]. Its spectral coverage is designed for this regime, and its combination of high multiplexing and a wide field of view will allow full coverage of the cluster virial regions—essential for conducting robust dynamical analyses. These observations will provide a unique dataset to investigate the assembly of mass and stars in massive clusters within their large-scale environments and to study the physical mechanisms that regulate star formation as a function of environment.

Acknowledgements. Funding for the Sloan Digital Sky Survey V has been provided by the Alfred P. Sloan Foundation, the Heising-Simons Foundation, the National Science Foundation, and the Participating Institutions. SDSS acknowledges support and resources from the Center for High-Performance Computing at the University of Utah. SDSS telescopes are located at Apache Point Observatory, funded by the Astrophysical Research Consortium and operated by New Mexico State University, and at Las Campanas Observatory, operated by the Carnegie Institution for Science. The SDSS web site is www.sdss.org. SDSS is managed by the Astrophysical Research Consortium for the Participating Institutions of the SDSS Collaboration, including Caltech, The Carnegie Institution for Science, Chilean National Time Allocation Committee (CNTAC) ratified researchers, The Flatiron Institute, the Gotham Participation Group, Harvard University, Heidelberg University, The Johns Hopkins University, L'Ecole polytechnique fédérale de Lausanne (EPFL), Leibniz-Institut für Astrophysik Potsdam (AIP), Max-Planck-Institut für Astronomie (MPIA Heidelberg), Max-Planck-Institut für Extraterrestrische Physik (MPE), Nanjing University, National Astronomical Observatories of China (NAOC), New Mexico State University, The Ohio State University, Pennsylvania State University, Smithsonian Astrophysical Observatory, Space Telescope Science Institute (STScI), the Stellar Astrophysics Participation Group, Universidad Nacional Autónoma de México, University of Arizona, University of Colorado Boulder, University of Illinois at Urbana-Champaign, University of Toronto, University of Utah, University of Virginia, Yale University, and Yunnan University.

GAMA is a joint European-Australasian project based around a spectroscopic campaign using the Anglo-Australian Telescope. The GAMA input catalogue is based on data taken from the Sloan Digital Sky Survey and the UKIRT Infrared Deep Sky Survey. Complementary imaging of the GAMA regions is being obtained by a number of independent survey programmes including GALEX MIS, VST KIDS, VISTA VIKING, WISE, Herschel-ATLAS, GMRT and ASKAP providing UV to radio coverage. GAMA is funded by the STFC (UK), the ARC (Australia), the AAO, and the participating institutions. The GAMA website is <http://www.gama-survey.org/>.

This paper uses data from the VIMOS Public Extragalactic Redshift Survey (VIPERS). VIPERS has been performed using the ESO Very Large Telescope, under the "Large Programme" 182.A-0886. The participating institutions and funding agencies are listed at <http://vipers.inaf.it>.

This work is based [in part] on observations made with the Spitzer Space Telescope, which was operated by the Jet Propulsion Laboratory, California Institute of Technology under a contract with NASA.

This work uses data from the ESO Programme 180.A-0776.

This research used data obtained with the Dark Energy Spectroscopic Instrument (DESI). DESI construction and operations is managed by the Lawrence Berkeley National Laboratory. This material is based upon work supported by the U.S. Department of Energy, Office of Science, Office of High-Energy Physics, under Contract No. DE-AC02-05CH11231, and by the National Energy Research Scientific Computing Center, a DOE Office of Science User Facility under the same contract. Additional support for DESI was provided by the U.S. National Science Foundation (NSF), Division of Astronomical Sciences under Contract No. AST-0950945 to the NSF's National Optical-Infrared Astronomy Research Laboratory; the Science and Technology Facilities Council of the United King-

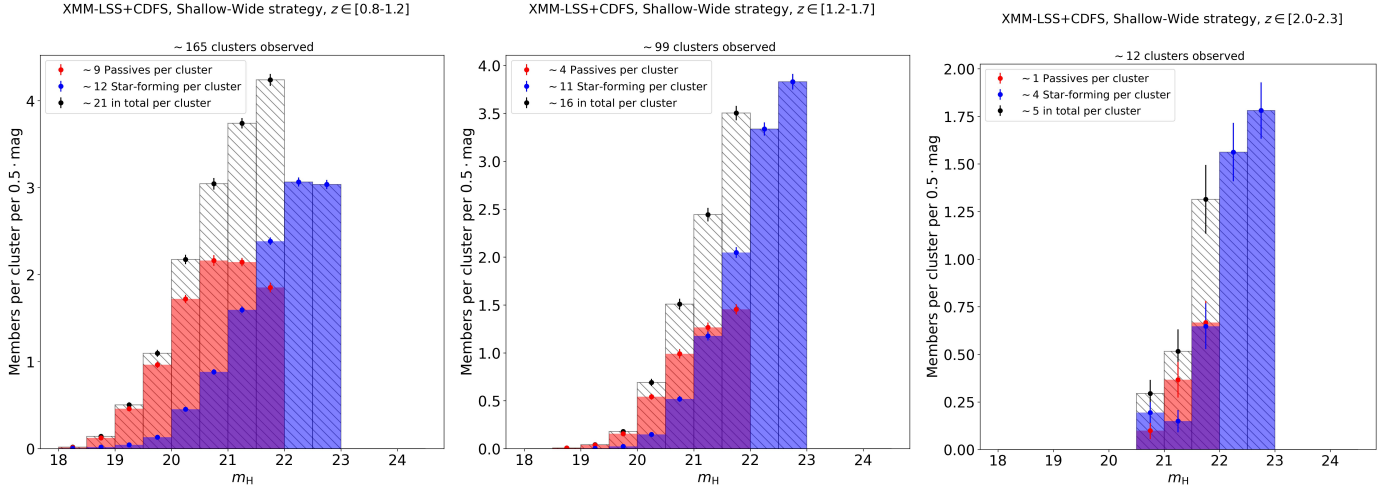


Fig. 17: Mean weighted distribution of the H-band magnitude of the detected members (in red for passive galaxies, in blue for star-forming galaxies. The dashed black bars are for all members) per cluster candidate when applying the Shallow-Wide MOONRISE strategy to the CDFS + XMM-LSS. From left to right, redshift ranges $[0.8, 1.2]$, $[1.2, 1.7]$ and $[2.0, 2.3]$ are shown. In each box, a legend describing the mean number of galaxies of different types expected to be observed by MOONRISE is added.

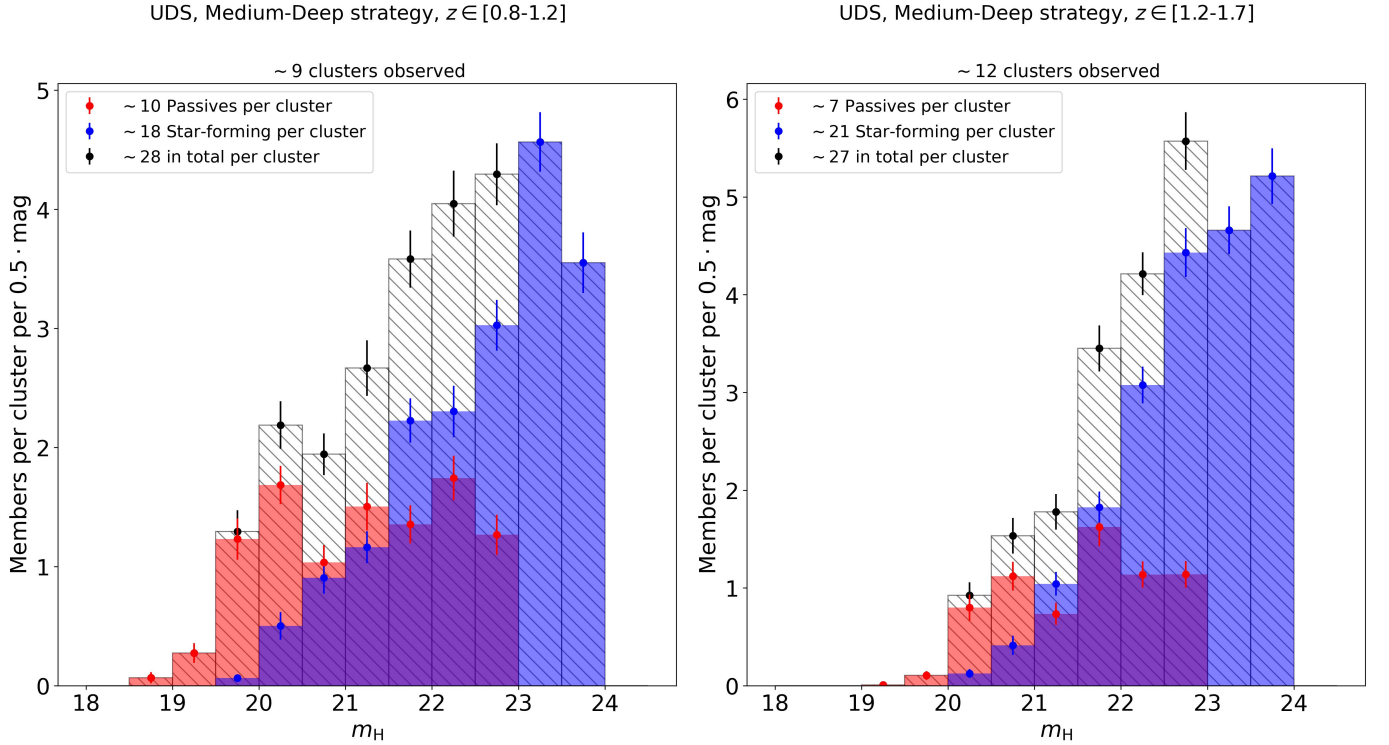


Fig. 18: Same as Fig.17 but for the UDS when applying the Medium-Deep strategy.

dom; the Gordon and Betty Moore Foundation; the Heising-Simons Foundation; the French Alternative Energies and Atomic Energy Commission (CEA); the National Council of Humanities, Science and Technology of Mexico (CONAH-CYT); the Ministry of Science and Innovation of Spain (MICINN), and by the DESI Member Institutions: www.desi.lbl.gov/collaborating-institutions. The DESI collaboration is honored to be permitted to conduct scientific research on l’oligam Du’ag (Kitt Peak), a mountain with particular significance to the Tohono O’odham Nation. Any opinions, findings, and conclusions or recommendations expressed in this material are those of the author(s) and do not necessarily reflect the views of the U.S. National Science Foundation, the U.S. Department of Energy, or any of the listed funding agencies.

This work is based on observations taken by the 3D-HST Treasury Program (GO 12177 and 12328) with the NASA/ESA HST, which is operated by the Association of Universities for Research in Astronomy, Inc., under NASA contract

NASS-26555.

GC acknowledges the support from the Next Generation EU funds within the National Recovery and Resilience Plan (PNRR), Mission 4 - Education and Research, Component 2 - From Research to Business (M4C2), Investment Line 3.1 - Strengthening and creation of Research Infrastructures, Project IR0000012 - “CTA+ - Cherenkov Telescope Array Plus”.

LM acknowledges the financial contribution from the PRIN-MUR 2022 20227RNLY3 grant “The concordance cosmological model: stress-tests with galaxy clusters” supported by Next Generation EU and from the grant ASI n. 2024-10-HH.0 “Attività scientifiche per la missione Euclid – fase E”

MV acknowledges financial support from the Inter-University Institute for Data Intensive Astronomy (IDIA), a partnership of the University of Cape Town, the University of Pretoria and the University of the Western Cape, and from the South African Department of Science and Innovation’s National Research

Foundation under the ISARP RADIOMAP Joint Research Scheme (DSI-NRF Grant Number 150551) and the CPRR HIPPO Project (DSI-NRF Grant Number SRUG22031677).

CB, PG and SM acknowledge financial support from the "Bonus Qualité Recherche" of Laboratoire J.L. Lagrange.

DJM acknowledges the support of the Royal Society through the award of a Royal Society University Research Professorship to Prof. James Dunlop.

This work was supported by the Swiss National Science Foundation (SNSF) under funding reference 200021_213076 "Galaxy evolution in the cosmic web".

References

- Adami, C., Durret, F., Benoist, C., et al. 2010, *A&A*, 509, A81
- Adami, C., Giles, P., Koulouridis, E., et al. 2018, *A&A*, 620, A5
- Aguena, M., Benoist, C., da Costa, L. N., et al. 2021, *Monthly Notices of the Royal Astronomical Society*, 502, 4435–4456
- Ahumada, R., Allende Prieto, C., Almeida, A., et al. 2020, *ApJS*, 249, 3
- Aihara, H., ALSayyad, Y., Ando, M., et al. 2019, *Publications of the Astronomical Society of Japan*, 71
- Andreon, S. 2003, *A&A*, 409, 37
- Andreon, S., Newman, A. B., Trinchieri, G., et al. 2014, *A&A*, 565, A120
- Andreon, S., Quintana, H., Tajer, M., Galaz, G., & Surdej, J. 2006, *MNRAS*, 365, 915
- Arnouts, S. & Ilbert, O. 2011, *LePHARE: Photometric Analysis for Redshift Estimate*
- Ashby, M. L. N., Willner, S. P., Fazio, G. G., et al. 2015, *ApJS*, 218, 33
- Ashby, M. L. N., Willner, S. P., Fazio, G. G., et al. 2013, *ApJ*, 769, 80
- Baldry, I. K., Liske, J., Brown, M. J. I., et al. 2018, *MNRAS*, 474, 3875
- Balogh, M. L., van der Burg, R. F. J., Muzzin, A., et al. 2020, *Monthly Notices of the Royal Astronomical Society*, 500, 358–387
- Becker, R. H., White, R. L., & Helfand, D. J. 1995, *ApJ*, 450, 559
- Beers, T. C., Flynn, K., & Gebhardt, K. 1990, *AJ*, 100, 32
- Bellagamba, F., Roncarelli, M., Maturi, M., & Moscardini, L. 2018, *MNRAS*, 473, 5221
- Benoist, C., Aguena, M., da Costa, L., et al. 2025, *arXiv e-prints*, [arXiv:2507.05360](https://arxiv.org/abs/2507.05360)
- Bertin, E. & Arnouts, S. 1996, *A&AS*, 117, 393
- Bleem, L. E., Stalder, B., de Haan, T., et al. 2015, *The Astrophysical Journal Supplement Series*, 216, 27
- Boquien, M., Burgarella, D., Roehly, Y., et al. 2019, *A&A*, 622, A103
- Bower, R. G., Lucey, J. R., & Ellis, R. S. 1992, *MNRAS*, 254, 601
- Bradshaw, E. J., Almaini, O., Hartley, W. G., et al. 2013, *Monthly Notices of the Royal Astronomical Society*, 433, 194–208
- Brammer, G. B., van Dokkum, P. G., & Coppi, P. 2008, *ApJ*, 686, 1503
- Brammer, G. B., van Dokkum, P. G., Franx, M., et al. 2012, *The Astrophysical Journal Supplement Series*, 200, 13
- Brodwin, M., Stanford, S. A., Gonzalez, A. H., et al. 2013, *ApJ*, 779, 138
- Bruzual, G. & Charlot, S. 2003, *MNRAS*, 344, 1000
- Bulbul, E., Liu, A., Kluge, M., et al. 2024, *A&A*, 685, A106
- Calvi, R., Castignani, G., & Dannerbauer, H. 2023, *A&A*, 678, A15
- Calzetti, D., Armus, L., Bohlin, R. C., et al. 2000, *ApJ*, 533, 682
- Carnall, A. C., McLure, R. J., Dunlop, J. S., et al. 2019, *Monthly Notices of the Royal Astronomical Society*, 490, 417–439
- Carnall, A. C., McLure, R. J., Dunlop, J. S., & Davé, R. 2018, *Monthly Notices of the Royal Astronomical Society*, 480, 4379–4401
- Castignani, G. & Benoist, C. 2016, *A&A*, 595, A111
- Castignani, G., Chiaberge, M., Celotti, A., & Norman, C. 2014a, *ApJ*, 792, 113
- Castignani, G., Chiaberge, M., Celotti, A., Norman, C., & De Zotti, G. 2014b, *ApJ*, 792, 114
- Castignani, G., Combes, F., Salomé, P., et al. 2019, *A&A*, 623, A48
- Cerulo, P., Couch, W. J., Lidman, C., et al. 2016, *Monthly Notices of the Royal Astronomical Society*, 457, 2209
- Chabrier, G. 2003, *Publications of the Astronomical Society of the Pacific*, 115, 763–795
- Chiaberge, M., Tremblay, G., Capetti, A., et al. 2009, *ApJ*, 696, 1103
- Chu, A., Durret, F., & Márquez, I. 2021, *A&A*, 649, A42
- Cirasuolo, M., Fairley, A., Rees, P., et al. 2020, *The Messenger*, 180, 10
- Colless, M., Dalton, G., Maddox, S., et al. 2001, *MNRAS*, 328, 1039
- Cooper, M. C., Yan, R., Dickinson, M., et al. 2012, *MNRAS*, 425, 2116
- De Lucia, G., Poggianti, B. M., Aragón-Salamanca, A., et al. 2007, *MNRAS*, 374, 809
- De Lucia, G., Springel, V., White, S. D. M., Croton, D., & Kauffmann, G. 2006, *MNRAS*, 366, 499
- DESI Collaboration, Abdul-Karim, M., Adame, A. G., et al. 2025, *Data Release 1 of the Dark Energy Spectroscopic Instrument*
- Doubrawa, L., Cypriano, E. S., Finoguenov, A., et al. 2024, *A&A*, 685, A98
- Dressler, A., Oemler, Jr., A., Couch, W. J., et al. 1997, *ApJ*, 490, 577
- Epinat, B., Contini, T., Mercier, W., et al. 2024, *A&A*, 683, A205
- Euclid Collaboration: Adam, R., Vannier, M., Maurogordato, S., et al. 2019, *A&A*, 627, A23
- Euclid Collaboration: Aussel, H., Tereno, I., Schirmer, M., et al. 2025, *arXiv e-prints*, [arXiv:2503.15302](https://arxiv.org/abs/2503.15302)
- Euclid Collaboration: Bhargava, S., Benoist, C., Gonzalez, A. H., et al. 2025, *arXiv e-prints*, [arXiv:2503.19196](https://arxiv.org/abs/2503.19196)
- Euclid Collaboration: Mellier, Y., Abdurro'uf, Acevedo Barroso, J. A., et al. 2025, *A&A*, 697, A1
- Euclid Collaboration: Moneti, A., McCracken, H. J., Shuntov, M., et al. 2022, *A&A*, 658, A126
- Euclid Collaboration: Scaramella, R., Amiaux, J., Mellier, Y., et al. 2022, *A&A*, 662, A112
- Finoguenov, A., Guzzo, L., Hasinger, G., et al. 2007, *ApJS*, 172, 182
- Finoguenov, A., Tanaka, M., Cooper, M., et al. 2015, *A&A*, 576, A130
- Fioc, M. & Rocca-Volmerange, B. 1997, *A&A*, 326, 950
- Fioc, M. & Rocca-Volmerange, B. 1999, *arXiv e-prints*, astro
- Furusawa, H., Kashikawa, N., Kobayashi, M. A. R., et al. 2016, *ApJ*, 822, 46
- Furusawa, H., Kosugi, G., Akiyama, M., et al. 2008, in *Astronomical Society of the Pacific Conference Series*, Vol. 399, *Panoramic Views of Galaxy Formation and Evolution*, ed. T. Kodama, T. Yamada, & K. Aoki, 131
- GAIA Collaboration, [url=https://dc.g-vo.org/gaia/q3/cone/info](https://dc.g-vo.org/gaia/q3/cone/info), h. 2020, *Gaia DR3 Lite Cone Search*
- Gavazzi, R. & Soucail, G. 2007, *A&A*, 462, 459
- Gladders, M. D. & Yee, H. K. C. 2000, *AJ*, 120, 2148
- Gunn, J. E. & Gott, III, J. R. 1972, *Astrophys. J.* 176: No. 1, 1–19 (15 Aug 1972).
- Hansen, S. M., McKay, T. A., Wechsler, R. H., et al. 2005, *ApJ*, 633, 122
- Hilton, M., Sifón, C., Naess, S., et al. 2021, *The Astrophysical Journal Supplement Series*, 253, 3
- Hudelot, P., Cuillandre, J. C., Withington, K., et al. 2012, *VizieR Online Data Catalog: The CFHTLS Survey (T0007 release) (Hudelot+ 2012)*, *VizieR Online Data Catalog: II/317*. Originally published in: *SPIE Conf. 2012*
- Hung, D., Lemaux, B. C., Gal, R. R., et al. 2020, *MNRAS*, 491, 5524
- Ilbert, O., Arnouts, S., McCracken, H. J., et al. 2006, *A&A*, 457, 841
- Ilbert, O., Capak, P., Salvato, M., et al. 2009, *ApJ*, 690, 1236
- Jaffé, Y. L., Aragón-Salamanca, A., De Lucia, G., et al. 2011, *MNRAS*, 410, 280
- Jarvis, M. J., Bonfield, D. G., Bruce, V. A., et al. 2013, *MNRAS*, 428, 1281
- Joo, H. & Jee, M. J. 2023, *Nature*, 613, 37
- Kellermann, K. I., Fomalont, E. B., Mainieri, V., et al. 2008, *The Astrophysical Journal Supplement Series*, 179, 71
- Kodama, T., Tanaka, I., Kajisawa, M., et al. 2007, *MNRAS*, 377, 1717
- Kroupa, P. 2001, *MNRAS*, 322, 231
- Kubo, M., Umehata, H., Matsuda, Y., et al. 2021, *ApJ*, 919, 6
- Lawrence, A., Warren, S. J., Almaini, O., et al. 2007, *MNRAS*, 379, 1599
- Le Fèvre, O., Vettolani, G., Garilli, B., et al. 2005, *A&A*, 439, 845
- Leroy, G., Pires, S., Pratt, G. W., & Giocoli, C. 2023, *A&A*, 678, A125
- Li, I. H., Yee, H. K. C., Hsieh, B. C., & Gladders, M. 2012, *ApJ*, 749, 150
- Lidman, C., Rosati, P., Demarco, R., et al. 2004, *A&A*, 416, 829
- Lidman, C., Rosati, P., Tanaka, M., et al. 2008, *A&A*, 489, 981
- Lidman, C., Tucker, B. E., Davis, T. M., et al. 2020, *MNRAS*, 496, 19
- Lin, Y.-T., Mohr, J. J., Gonzalez, A. H., & Stanford, S. A. 2006, *ApJ*, 650, L99
- López-Cruz, O., Barkhouse, W. A., & Yee, H. K. C. 2004, *ApJ*, 614, 679
- Maiolino, R., Cirasuolo, M., Afonso, J., et al. 2020, *Published in The Messenger* vol. 180, pp. 24–29, June 2020.
- Mao, M. Y., Sharp, R., Norris, R. P., et al. 2012, *MNRAS*, 426, 3334
- Maturi, M., Bellagamba, F., Radovich, M., et al. 2019, *MNRAS*, 485, 498
- Maturi, M., Finoguenov, A., Lopes, P. A. A., et al. 2023, *A&A*, 678, A145
- Maturi, M., Meneghetti, M., Bartelmann, M., Dolag, K., & Moscardini, L. 2005, *A&A*, 442, 851
- Maturi, M., Radovich, M., Moscardini, L., et al. 2025, *arXiv e-prints*, [arXiv:2507.14338](https://arxiv.org/abs/2507.14338)
- Mauduit, J. C., Lacy, M., Farrah, D., et al. 2012, *PASP*, 124, 714
- McConachie, I., Wilson, G., Forrest, B., et al. 2022, *ApJ*, 926, 37
- McLeod, D. J., McLure, R. J., Dunlop, J. S., et al. 2021, *MNRAS*, 503, 4413
- McLure, R. J., Pearce, H. J., Dunlop, J. S., et al. 2013, *MNRAS*, 428, 1088
- Mehta, V., Scarlata, C., Capak, P., et al. 2018, *ApJS*, 235, 36
- Mei, S., Holden, B. P., Blakeslee, J. P., et al. 2009, *ApJ*, 690, 42
- Merlin, E., Fontana, A., Ferguson, H. C., et al. 2015, *A&A*, 582, A15
- Miller, C. J., Nichol, R. C., Reichart, D., et al. 2005, *AJ*, 130, 968
- Miyazaki, S., Hamana, T., Ellis, R. S., et al. 2007, *ApJ*, 669, 714
- Miyazaki, S., Hamana, T., Shimasaku, K., et al. 2002, *ApJ*, 580, L97
- Momcheva, I. G., Brammer, G. B., van Dokkum, P. G., et al. 2016, *The Astrophysical Journal Supplement Series*, 225, 27
- Mortlock, D. J., Madgwick, D. S., & Lahav, O. 2001, *Publications of the Astronomical Society of Australia*, 18, 192–194
- Myles, J., Gruen, D., Jeltama, T., et al. 2025, *MNRAS*, 544, 2080
- Ni, Q., Brandt, W. N., Chen, C.-T., et al. 2021, *VizieR Online Data Catalog: XMM-SERVS survey: X-ray sources for W-CDF-S & ELAIS-S1 (Ni+, 2021)*, *VizieR On-line Data Catalog: J/ApJS/256/21*. Originally published in: 2021ApJS...256...21N

- Ni, Q., Timlin, J., Brandt, W. N., & Yang, G. 2019, *Research Notes of the American Astronomical Society*, 3, 5
- Noordeh, E., Canning, R. E. A., Willis, J. P., et al. 2021, *Monthly Notices of the Royal Astronomical Society*, 507, 5272
- Oguri, M., Lin, Y.-T., Lin, S.-C., et al. 2018, *PASJ*, 70, S20
- Oguri, M. & Takahashi, R. 2022, *Phys. Rev. D*, 106, 043532
- Pacaud, F., Clerc, N., Giles, P. A., et al. 2016, *A&A*, 592, A2
- Papovich, C., Momcheva, I., Willmer, C. N. A., et al. 2010, *The Astrophysical Journal*, 716, 1503–1513
- Pentericci, L., McLure, R. J., Garilli, B., et al. 2018, *A&A*, 616, A174
- Pharo, J., Malhotra, S., Rhoads, J. E., et al. 2020, *ApJ*, 888, 79
- Planck Collaboration, Ade, P. A. R., Aghanim, N., et al. 2016, *A&A*, 594, A27
- Robotham, A. S. G., Norberg, P., Driver, S. P., et al. 2011, *MNRAS*, 416, 2640
- Rykoff, E. S., Rozo, E., Busha, M. T., et al. 2014, *The Astrophysical Journal*, 785, 104
- Scodreggio, M., Guzzo, L., Garilli, B., et al. 2018, *A&A*, 609, A84
- Shi, D., Wang, X., Zheng, X., et al. 2023, *The Emergence of Brightest Cluster Galaxy in a Protocluster Core at $z = 2.24$*
- Stanford, S. A., Brodwin, M., Gonzalez, A. H., et al. 2012, *ApJ*, 753, 164
- Stott, J. P., Pimbblet, K. A., Edge, A. C., Smith, G. P., & Wardlow, J. L. 2009, *MNRAS*, 394, 2098
- Strazzullo, V., Pannella, M., Mohr, J. J., et al. 2019, *A&A*, 622, A117
- Tasca, L. A. M., Le Fèvre, O., Ribeiro, B., et al. 2017, *A&A*, 600, A110
- Tempel, E., Tago, E., & Liivamägi, L. J. 2012, *A&A*, 540, A106
- Thongkham, K., Gonzalez, A. H., Brodwin, M., et al. 2024, *ApJ*, 967, 123
- Toni, G., Gozaliasl, G., Maturi, M., et al. 2025a, *A&A*, 697, A197
- Toni, G., Maturi, M., Castignani, G., et al. 2025b, *arXiv e-prints*, arXiv:2509.08040
- Toni, G., Maturi, M., Finoguenov, A., Moscardini, L., & Castignani, G. 2024, *A&A*, 687, A56
- Trudeau, A., Garrel, C., Willis, J., et al. 2020, *A&A*, 642, A124
- Urrutia, T., Wisotzki, L., Kerutt, J., et al. 2019, *A&A*, 624, A141
- Vaccari, M., Covone, G., Radovich, M., et al. 2016, in *The 4th Annual Conference on High Energy Astrophysics in Southern Africa (HEASA 2016)*, 26
- Valentinuzzi, T., Poggianti, B. M., Fasano, G., et al. 2011, *A&A*, 536, A34
- van Dokkum, P. G., Franx, M., Fabricant, D., Kelson, D. D., & Illingworth, G. D. 1999, *ApJ*, 520, L95
- Wang, W.-H., Foucaud, S., Hsieh, B.-C., et al. 2022, *arXiv e-prints*, arXiv:2205.11546
- Wang, X., Jones, T. A., Treu, T., et al. 2017, *ApJ*, 837, 89
- Werner, S. V., Hatch, N. A., Matharu, J., et al. 2023, *MNRAS*, 523, 91
- Willis, J. P., Canning, R. E. A., Noordeh, E. S., et al. 2020, *Nature*, 577, 39
- Wylezalek, D., Galametz, A., Stern, D., et al. 2013, *ApJ*, 769, 79
- Yang, X., Mo, H. J., van den Bosch, F. C., et al. 2007, *ApJ*, 671, 153
- ¹² INAF-IAPS, Via Fosso del Cavaliere 100, I-00133 Roma, Italy
- ¹³ ESO
- ¹⁴ Department of Physics “E. Pancini”, University of Naples Federico II, Naples, Italy
- ¹⁵ INAF – Osservatorio Astronomico di Capodimonte, Salita Moiarriello 16, I-80131, Napoli, Italy
- ¹⁶ INFN, Sezione di Napoli, Via Cintia, I-80126 Napoli, Italy
- ¹⁷ Department of Astronomy, University of Geneva, ch. d’Ecogia 16, CH-1290 Versoix, Switzerland
- ¹⁸ Kavli Institute for Cosmology, University of Cambridge, Madingley Road, Cambridge CB3 0HA, UK
- ¹⁹ Cavendish Laboratory – Astrophysics Group, University of Cambridge, 19 JJ Thomson Avenue, Cambridge CB3 0HE, UK
- ²⁰ Department of Physics and Astronomy, University College London, Gower Street, London WC1E 6BT, UK
- ²¹ CSST Science Center for Guangdong-Hong Kong-Macau Great Bay Area, 519082 Zhuhai, PR China
- ²² School of Physics and Astronomy, Sun Yat-sen University Zhuhai Campus, 2 Daxue Road, Tangjia, Zhuhai, Guangdong 519082, PR China
- ²³ INAF - Istituto di Radioastronomia, via Gobetti 101, 40129 Bologna, Italy
- ²⁴ Inter-University Institute for Data Intensive Astronomy, Department of Astronomy, University of Cape Town, 7701 Rondebosch, Cape Town, South Africa
- ²⁵ Inter-University Institute for Data Intensive Astronomy, Department of Physics and Astronomy, University of the Western Cape, 7535 Bellville, Cape Town, South Africa

- ¹ Université Côte d’Azur, Observatoire de la Côte d’Azur, CNRS, Laboratoire Lagrange, Bd de l’Observatoire, CS 34229, 06304 Nice cedex 4, France
- ² INAF - Osservatorio di Astrofisica e Scienza dello Spazio di Bologna, via Gobetti 93/3, I-40129, Bologna, Italy
- ³ Center for Astronomy - University of Heidelberg, Albert-Ueberle-Straße 2, 69120 Heidelberg, Germany
- ⁴ Institute of Theoretical Physics - University of Heidelberg, Albert-Ueberle-Straße 2, 69120 Heidelberg, Germany
- ⁵ Laboratoire d’astrophysique, École Polytechnique Fédérale de Lausanne (EPFL), Chemin Pegasi 51, 1290 Versoix, Switzerland
- ⁶ LUX, Observatoire de Paris, Université PSL, CNRS, Place Jules Janssen, F-92195 Meudon, France
- ⁷ School of Physics and Astronomy, University of Nottingham, University Park, Nottingham NG7 2RD, UK
- ⁸ Institute for Astronomy, University of Edinburgh, Royal Observatory, Edinburgh, EH9 3HJ, UK
- ⁹ Jodrell Bank Centre for Astrophysics, Department of Physics and Astronomy, School of Natural Sciences, The University of Manchester, Manchester, M13 9PL, UK
- ¹⁰ Dipartimento di Fisica e Astronomia “Augusto Righi”, Alma Mater Studiorum Università di Bologna, Via Gobetti 93/2, I-40129 Bologna, Italy
- ¹¹ INFN - Sezione di Bologna, Viale Berti Pichat 6/2, 40127 Bologna, Italy

Appendix A Spectroscopic properties

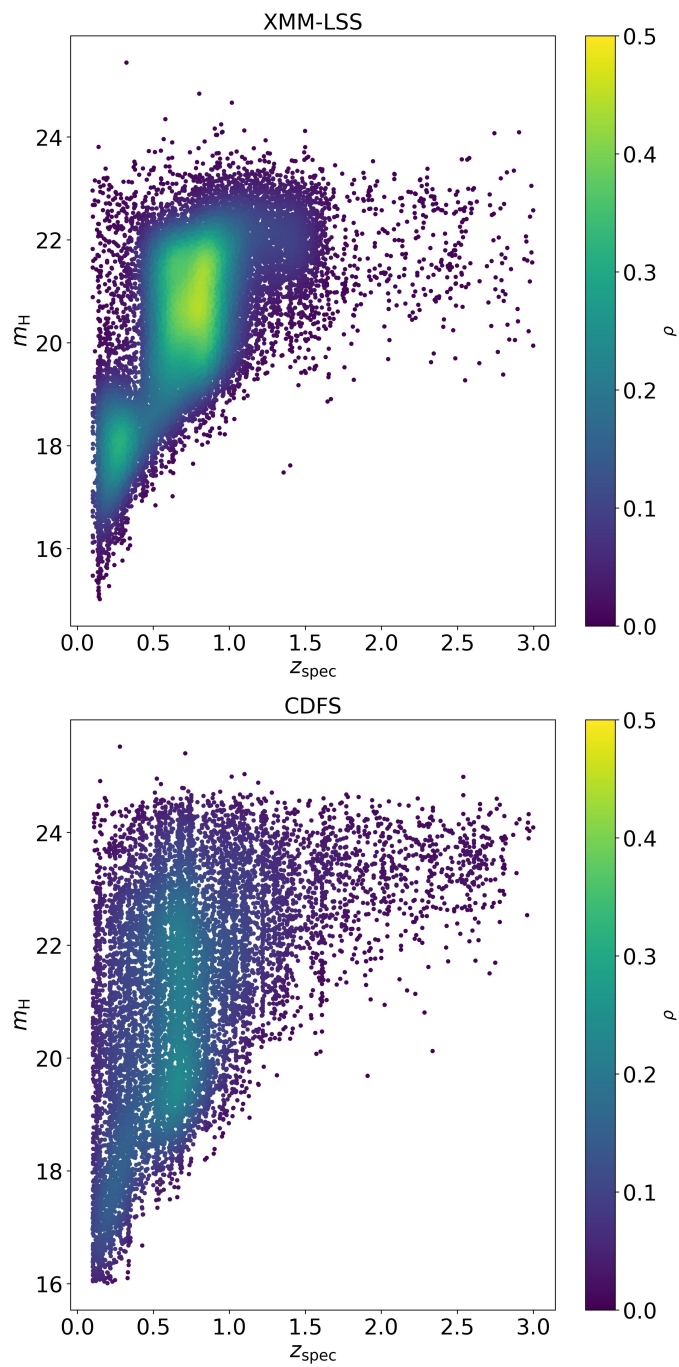


Fig. A.1: Redshift- m_H relation for galaxies with spectroscopic redshift in the XMM-LSS (top panel) and CDFS (bottom panel). The colour maps represent the amplitude of the probability density function of the points distribution.

Appendix B Cluster catalogues

Table B.1: First 5 AMICO-WaZP joint cluster candidates within the XMM-LSS.

ID	RA	Dec	z_{phot}	$\text{rich}_{\text{WaZP}}$	$\text{rich}_{\text{AMICO}}$	S/N_{WaZP}	S/N_{AMICO}	$z_{\text{spec, mem}}$	$N_{z\text{spec}}$	$z_{\text{spec, BCG}}$	Coverage fraction (%)
0	33.8711	-4.6807	0.37	78.95	48.22	21.64	35.38	0.35	18	0.348	80
1	35.7645	-4.604	1.2	39.6	46.29	20.51	41.03	Nan	Nan	Nan	91
2	37.1303	-4.7336	0.61	68.83	40.18	17.37	28.63	0.611	19	0.612	100
3	34.9847	-5.4697	0.33	23.76	19.81	17.09	21.25	0.28	15	0.278	100
4	37.1202	-4.9964	0.39	27.47	25.93	15.68	24.08	0.333	6	0.334	100

Table B.2: First 5 AMICO-WaZP joint cluster candidates within the CDFS.

ID	RA	Dec	z_{phot}	$\text{rich}_{\text{WaZP}}$	$\text{rich}_{\text{AMICO}}$	S/N_{WaZP}	S/N_{AMICO}	$z_{\text{spec, mem}}$	$N_{z\text{spec}}$	$z_{\text{spec, BCG}}$	Coverage fraction (%)
0	53.5646	-28.4127	0.66	136.45	60.64	19.26	37.81	0.664	9	Nan	99
1	53.4671	-27.3556	0.59	62.51	51.53	18.7	41.38	0.606	6	0.604	98
2	52.0146	-27.4462	1.2	32.04	28.52	15.84	28.18	Nan	Nan	Nan	88
3	52.374	-28.3276	0.67	77.86	51.53	15.62	38.51	0.682	7	Nan	86
4	52.8823	-28.7031	0.9	51.63	30.1	15.58	18.26	Nan	Nan	0.849	99

^a Tables ordered by decreasing order of WaZP S/N. See Sect.4 for columns description.

Appendix C Spurious associations with clusters from the literature

In this Appendix, we describe the 4 cases of cluster candidates with a redshift offset larger than 0.06 relative to the matched cluster catalogue taken from the literature, as discussed in Sect.5.4.

- **SXDF49XGG, from Balogh et al. 2020:**

- $z_{\text{lit}} = 1.091$
- Matched with C1104, with a measured $z_{\text{phot, joint}} \sim 1.39$
- C1104 is also matched with SXDF87XXGG with $z_{\text{lit}} = 1.406$.
- C1104 is closer to SXDF87XXGG than SXDF49XGG
- SXDF49XGG has a velocity dispersion of $255 \pm 50 \text{ km} \cdot \text{s}^{-1}$, while SXDF87XXGG has an estimated velocity dispersion of $700 \pm 110 \text{ km} \cdot \text{s}^{-1}$

Conclusion: the match between C1104 and SXDF49XGG could be a spurious association along the line of sight with a low mass, foreground group of galaxies, while the most likely counterpart to C1104 possibly is SXDF87XXGG.

- **XLSSC-191, from Adami et al. 2018:**

- $z_{\text{lit}} = 0.05$
- Matched with C1136, with a measured $z_{\text{phot, joint}} \sim 0.15$.
- We also have $z_{\text{spec, gaussian}} = 0.147$, using 39 members.
- XLSSC-191 has a low mass ($R_{500, X} \sim 491 \text{ kpc}$, $M_{500, X} \sim 0.3 \times 10^{14} M_{\odot}$)

Conclusion: the match between C1136 and XLSSC-191 could be a spurious association along the line of sight with a low mass, foreground group of galaxies.

- **J033223.2-274943, from Finoguenov et al. 2015:**

- $z_{\text{lit}} = 0.578$, computed with 5 members within R_{200}
- Matched with C1169, with a measured $z_{\text{phot, joint}} \sim 0.71$
- We also have $z_{\text{spec, gaussian}} = 0.734$, using 30 members.
- Significant angular separation between them ($\sim 2 \text{ arcmin}$, i.e, a projected physical separation of $\sim 800 \text{ kpc}$ at the median redshift)

Conclusion: Possibly our estimation of the spectroscopic redshift of this structure is more robust, but we cannot exclude the possibility of a spurious association with a different structure along the line of sight, as their angular separation is large.

- **J033136.7-275233, from Finoguenov et al. 2015:**

- $z_{\text{lit}} = 1.05$
- Matched with C145, with a measured $z_{\text{phot, joint}} \sim 1.21$
- Small angular separation between them ($\sim 0.3 \text{ arcmin}$, corresponding to a projected physical separation of $\sim 160 \text{ kpc}$ at the median redshift)
- No significant concentration of galaxies in the photometric redshift distribution at $z = 1.05$ within a window of 1 arcmin centred at the C145 location.
- Low mass system ($\sigma_v \sim 280 \text{ km} \cdot \text{s}^{-1}$)

Conclusion: it could possibly be a random association with a poor foreground group of galaxies not detected by our algorithms.